Boundary Frustration in Double-Gyroid Thin

Films

Benjamin R. Magruder, David C. Morse, Christopher J. Ellison, and Kevin D.

Dorfman*

Department of Chemical Engineering and Materials Science, University of Minnesota Twin

Cities, 421 Washington Avenue SE, Minneapolis, Minnesota 55455, USA

E-mail: dorfman@umn.edu

Abstract

Self-consistent field theory for thin films of AB diblock polymers in the doublegyroid phase reveals that, in the absence of preferential wetting of monomer species at the film boundaries, films with the (211) plane oriented parallel to the boundaries are more stable than other orientations, consistent with experimental results. This preferred orientation is explained in the context of boundary frustration. Specifically, the angle of intersection between the A/B interface and the film boundary—the wetting angle—is thermodynamically restricted to a narrow range of values. Most termination planes in double gyroid cannot accommodate this narrow range of wetting angles without significant local distortion relative to the bulk morphology; the (211)-oriented termination plane with the "double-wave" pattern produces relatively minimal distortion, making it the least frustrated boundary. The principle of boundary frustration provides a framework to understand the relative stability of termination planes for complex ordered block polymer phases confined between flat, nonpreferential boundaries.

Many promising applications of self-assembled block polymers, including their use as nanolithographic templates, ^{1–5} nanoporous membranes, ^{6–11} and advanced optical and electronic material templates, ^{11–18} require thin-film confinement. The double-gyroid (DG) phase in thin films has received particular interest recently because of its potential utility in these applications. ^{17–26} For instance, DG has been proposed as a template for optical metamaterials, whose circular dichroism is predicted to vary with the termination plane at the film's exposed surface. ¹⁸ DG has also been considered for filtration membranes ⁸ and as a template for electronic materials ¹⁶ owing to its uniform domain size and three-dimensionally co-continuous morphology. However, the effects of thin-film confinement on DG are poorly understood.

Boundary effects in thin films alter both the morphologies and stability windows of block-polymer phases relative to the bulk.^{3–5,27} The most consequential boundary effect is preferential wetting, which biases the system toward a phase and orientation that maximizes the area fraction of the preferred species at the boundary.^{27–32} This effect can result in contact energies that dominate over all other contributions to the free energy.³³ Experimentally realizing DG thin films has been limited to relatively nonpreferential interfaces; ^{19–26} when polymers that form DG in the bulk are placed between highly preferential boundaries, they instead form other phases ^{32,34–36} or mixed morphologies ³⁷ that allow for the formation of a complete wetting layer at the film boundary. Owing to this practical constraint, we primarily focus here on nonpreferential boundaries.

Prior work on lamella- and cylinder-forming systems has revealed four additional boundary effects that are also important to thin-film phase behavior, especially in the absence of preferential wetting. First, commensurability between the film thickness and the bulk domain spacing affects the relative stability of different orientations of each phase. ^{28–31} Incommensurate film thicknesses can cause the film to separate into terraced regions of different thicknesses ^{28,38–40} and can sometimes stabilize an entirely different phase. ^{32,41,42} Second, chain ends are entropically preferred near the film boundaries, causing a small preference for

the minority block at these boundaries since minority-block domains have a higher density of chain ends. $^{29,43-47}$ Third, the reduced polymer density at the boundary lowers the A/B interaction energy, causing a negative line tension that favors intersections between the A/B interface and the film boundary. 28,30,47 And fourth, in a diblock with conformational asymmetry, the block with the smaller statistical segment length is entropically favored at the film boundary. $^{48-50}$

These effects are sufficient to explain the behavior of lamellar and cylindrical phases in thin films. 3-5,27 However, DG films demonstrate an additional boundary effect not present in these other phases, which we will call boundary frustration. For a film with nonpreferential boundaries, favorable locations for termination planes in the bulk morphology are the planes in which the polymers, on average, either lie parallel to the plane (as for perpendicular lamellae) or terminate at the plane (as for parallel lamellae), so that the presence of a film boundary minimally disrupts the bulk morphology. Planes of mirror symmetry in a bulk structure always satisfy these criteria, and are thus natural locations for termination planes. 51 Most common block polymer phases have mirror planes, so they have no boundary frustration. However, DG does not have any mirror planes, nor any other planes that satisfy the above criteria. So, to accommodate the film boundaries, a DG thin film must be distorted relative to the bulk, with a different (and likely broader) distribution of chain stretching than the bulk morphology. Neither the nature of these distortions nor their effect on the stability of different termination planes has been studied. Indeed, DG thin films in experiments almost always form with one particular termination plane at both interfaces of the film—the (211)-oriented plane containing the so-called "double-wave" pattern ^{19–26}—but an explanation for the ubiquity of this termination plane has remained elusive. Furthermore, most DG thin films have been fabricated using solvent vapor annealing, ^{19–24} which alters chemical interactions and often traps nonequilibrium structures, ^{52,53} so these experiments may not always be exhibiting equilibrium behavior.

In this study, we modeled the effects of boundary frustration to explain why the (211)

orientation is favored in DG thin films. We use self-consistent field theory $(SCFT)^{54}$ to calculate the equilibrium morphology and free energy of various DG thin films, using the masking method originally formulated by Matsen²⁸ to model confinement between two rigid boundaries (hereafter referred to as "walls"). Although these calculations model confinement between two walls, they are equally relevant for describing films that are open to air: a common-tangent construction can be used to predict terrace formation in open-air films based on the free energies of films confined between two walls. 28 Our model system contains a conformationally symmetric diblock polymer in the intermediate segregation regime that forms DG in the bulk: a polymer with segregation strength $\chi N = 20$ and A-block volume fraction $f_A = 0.36$. To model interfacial wetting, we define a Flory-Huggins-like interaction parameter $\chi_{\alpha W}$ such that the product $\chi_{\alpha W}N$ defines the segregation strength between each monomer species α and the walls, where N is the degree of polymerization of the polymer.⁵⁵ All data are calculated with identical walls, so $\chi_{\alpha W}$ describes interactions with both the top and bottom walls. This model is somewhat simplified relative to experimental systems, allowing us to isolate the effect of boundary frustration from the effects of other confounding variables like conformational asymmetry or asymmetric wetting at the film boundaries. The ability to impose thin-film confinement has been added as a feature in the open-source PSCF software, 56,57 which was used to perform this study. The details of our implementation of thin-film SCFT are given in the Supporting Information.

To describe arbitrary planes through a crystallographic unit cell, we introduce the following notation: $(hkl)_{\tau}$ denotes the plane parallel to the (hkl) lattice plane that is a distance τd_{hkl} from the origin of the unit cell, where h, k, and l are integer indices and d_{hkl} is the d-spacing between adjacent (hkl) planes. To remove any ambiguity, we always use the smallest integer set of hkl indices (i.e., divide by any common integer factors). We also restrict τ to values in the range [0,1) when referring to a single plane, since the planes at τ and $\tau+1$ are always symmetry-equivalent by a translation along the simple cubic Bravais lattice. The DG space group, $Ia\bar{3}d$, has only one standard choice of origin, so this notation is fully

defined. As an important example, the (211)-oriented plane with the double-wave pattern, sometimes called the (422) plane, 26,58 is denoted as $(211)_{1/2}$ in this notation.

We began by constructing a set of initial guesses with various termination planes, and performed an SCFT calculation for each guess. The initial guesses were constructed from the converged SCFT solution for DG in the bulk. The composition profile of the bulk phase was rotated and expanded/truncated to position the desired termination planes at the walls, and the resulting composition profile was converted to SCFT potential fields using the method described in the Supporting Information. To ensure that each calculation had the same termination plane on both walls, we enforced space-group symmetry throughout the calculation, and we ensured that each film had a symmetry operation—either inversion or rotation—relating the top half of the film to the bottom half. Film thicknesses in this initial set of calculations were between $0.8a_{\rm bulk}$ and $1.7a_{\rm bulk}$, where $a_{\rm bulk}$ is the bulk DG lattice parameter. Though these films are thinner than any DG films observed experimentally, ^{19–26} these thicknesses were chosen because they capture all relevant boundary effects (as will be shown below) while minimizing computational expense. To model nonpreferential walls, we set $\chi_{AW}N = \chi_{BW}N = 0$. We restrict our guesses to the four orientations observed experimentally: ^{25,59} films with the (211), (110), (111), and (001) lattice planes parallel to the wall. Specifically, the termination planes tested were $(211)_{n/8}$, $(110)_{n/16}$, $(111)_{n/16}$, and $(001)_{n/32}$, where n = 0, 1, 2, ..., 8. These planes were chosen because, in each orientation, the n=0 and n=8 planes are symmetry-equivalent in the $Ia\bar{3}d$ space group; thus, consideration of planes with n > 8 would be redundant with a calculation at lower n, as demonstrated in the Supporting Information.

Many of these SCFT calculations either converged to a solution with a different termination plane than the initial guess or converged to a defective structure, indicating that many of the initial guesses tested do not correspond to physically plausible thin films. A visualization of each initial guess and its converged solution is included in the Supporting Information (Figures S2-S5). The four termination planes that have been observed experi-

mentally 25,59 —the $(211)_{1/2}$, $(001)_{1/8}$, $(111)_0$, and $(110)_{1/4}$ planes—were among the converged solutions that we observed, and they are the most stable thin films in their respective orientations, as described further below. Films with these four termination planes are shown in Figure 1. Note that any plane that is symmetry-equivalent to these planes is an identical termination plane, and the periodicity of these symmetry-equivalent planes differs in each orientation. The complete sets of symmetry-equivalent planes matching the four planes in Figure 1 are $(211)_{m/2}$, $(001)_{m/8}$, $(111)_{n/4}$, and $(110)_{m/4}$, where m is any odd integer and n is any integer (see Supporting Information).

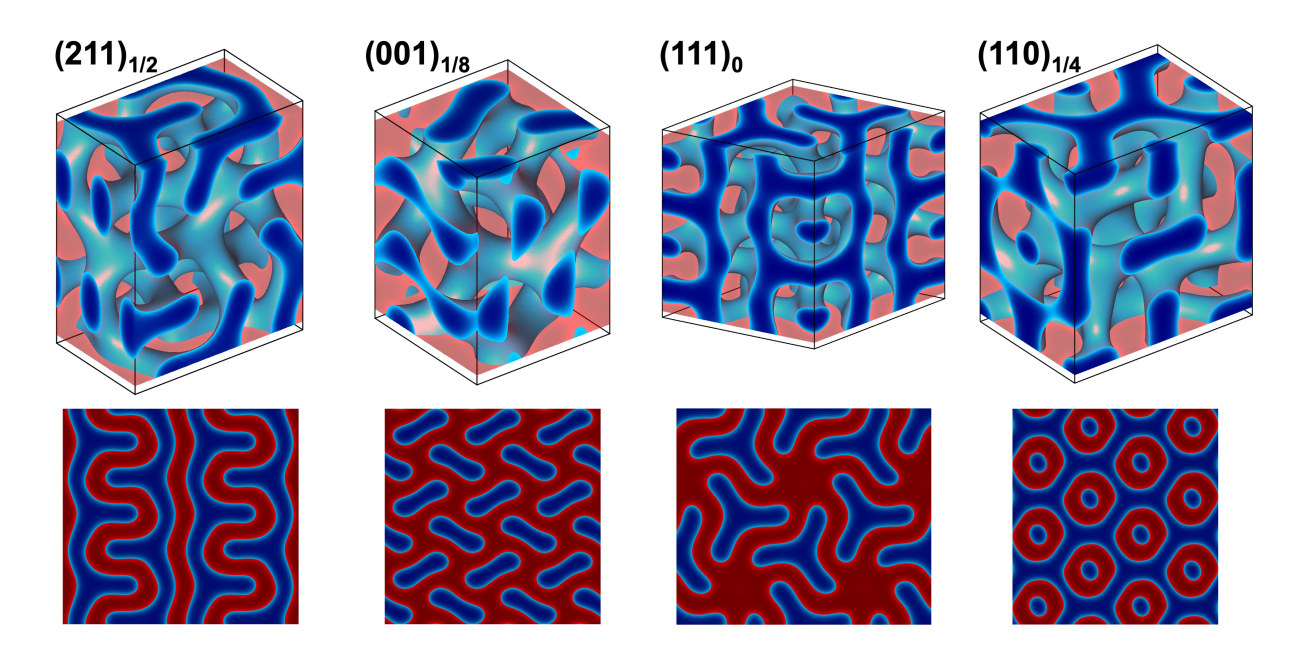


Figure 1: Converged SCFT solutions for thin films of the double-gyroid phase. For these calculations, $f_A = 0.36$, $\chi N = 20$, and the walls are nonpreferential ($\chi_{AW}N = \chi_{BW}N = 0$). The termination plane for each solution is given above the corresponding images. For each solution, a 3D composition profile of a single unit cell is shown (top row), along with a 2D profile of the polymer domain pattern at the polymer/wall interface (bottom row). Colors indicate the volume fraction of species A and B, where dark blue indicates a high concentration of species A and dark red indicates a high concentration of B. The transparent region at the top and bottom of each unit cell is the space occupied by the walls in the SCFT calculation. All boundaries shown are periodic. An alternate version of this figure containing colorbars and axis tick marks is given in Figure S6. Images are not presented to scale with one another. Note that $(211)_{1/2}$ denotes the (211)-oriented plane with the double-wave pattern.

For each converged SCFT solution, we then varied the film thickness and calculated the

free energy at each state point to identify the optimal film thickness and corresponding free energy minimum. The four films shown in Figure 1 were the most stable in their respective orientations. For these four termination planes, we extended our calculations further to consider all film thicknesses between $0.6a_{\text{bulk}}$ and $2.2a_{\text{bulk}}$. The resulting free energy profiles are shown in Figure 2, revealing that $(211)_{m/2}$ termination planes are the most stable. Additionally, as thickness increases, the free energy profiles continue to follow the same general behavior, indicating that our calculations at low thicknesses capture the same boundary effects that exist in thicker films. The shapes of these free energy profiles resemble those of thin films of parallel-oriented lamellae, described in detail elsewhere. Briefly, the periodicity of the local minima in each free energy profile matches the periodicity of the termination planes in the bulk, and the free energy rapidly increases at thicknesses above and below these minima because the structure becomes stretched or compressed to maintain the same termination planes at nonoptimal thicknesses. The local maxima in the free energy profiles correspond to changes in the number of periods within the film.

To provide a structural explanation for the stability of the $(211)_{m/2}$ termination planes, we return to the idea of boundary frustration. Each termination plane is unique in its boundary frustration, requiring different distortions to accommodate a rigid wall. Furthermore, in the absence of preferential wetting, boundary frustration is the dominant contributor to DG thin film stability, because the other boundary effects discussed in the context of lamella- and cylinder-forming thin films cannot account for significant energetic differences between DG termination planes, as shown in the Supporting Information.

Distortions arising due to boundary frustration will alter the shape of the A/B interface relative to the bulk. Here, we define the A/B interface as the surface on which species A and B have equal volume fractions. Correspondingly, the wall is represented by the midplane of the finite-width polymer/wall interface. Inspection of the A/B interfaces in our SCFT solutions reveals that they all share a common feature: the angle of intersection between the A/B interface and the wall is narrowly distributed around 85°, angled toward the minority

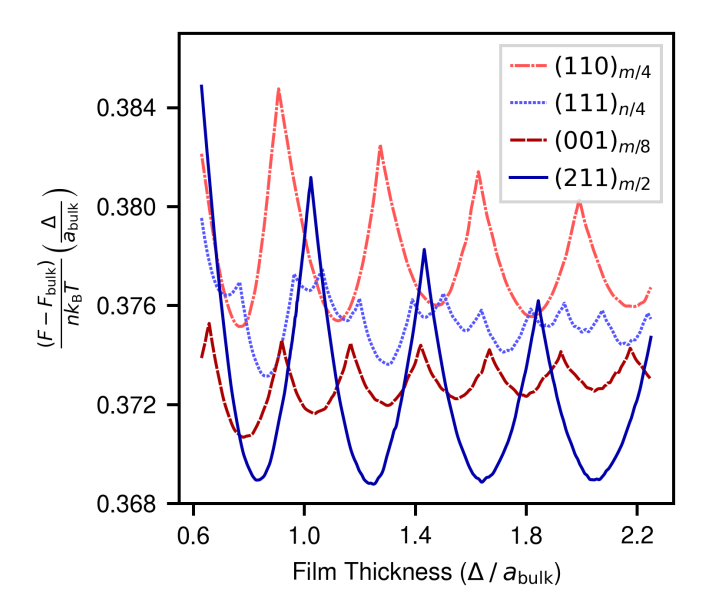


Figure 2: Excess free energy of the double-gyroid phase relative to the bulk $(F - F_{\text{bulk}})$ per polymer per unit area, plotted as a function of film thickness (Δ/a_{bulk}) for each of the four sets of termination planes indicated by the legend (where a_{bulk} is the lattice parameter for the DG unit cell in the bulk). In the legend, m denotes an odd integer and n denotes an integer. For these calculations, $f_{\text{A}} = 0.36$, $\chi N = 20$, and the walls are nonpreferential $(\chi_{\text{AW}}N = \chi_{\text{BW}}N = 0)$. The individual data points used to construct this figure are shown in Figure S7.

domain. This is true at every point of contact between the A/B interface and the wall across all converged solutions, even for phases other than DG that we tested, as demonstrated in Figure S9. Distortions at a frustrated boundary thus occur in order to achieve this nearly-constant wetting angle against the wall. Previous studies support this observation, showing that the wetting angles for cylinders and lamellae are less than 90° when $f_A < 0.5$. ^{29,43–47} The cylinders and lamellae widen against the wall to increase the minority block area fraction, which has a higher chain-end density and is entropically favored. However, the wetting angle itself has not previously been noted as an important parameter.

Presumably, the most stable DG thin films are those that exhibit the least distortion relative to the bulk. Thus, a plane through the bulk DG morphology should be a favorable termination plane if the plane intersects the A/B interface at angles narrowly distributed around 85°, since the distortions required to accommodate a wall on this plane will be relatively small. To make this more quantitative, let θ_z denote the angle between the A/B

interface and the film's bottom wall, where the angle is measured on the minority-domain (A) side of the A/B interface. The A/B interface thus forms an angle of $180^{\circ} - \theta_z$ with the film's top wall. Analogously, in the bulk morphology, let θ_z refer to the angle between the A/B interface and some plane (hkl) that defines the orientation. Figure 3 shows how the distribution of θ_z varies in the (211) and (111) orientations throughout both the bulk and thin film morphologies. The data are presented as normalized 2D histograms, in which the entire A/B interface is sorted into bins represented by the pixels on each figure. The procedure for generating Figure 3 is described in the Supporting Information.

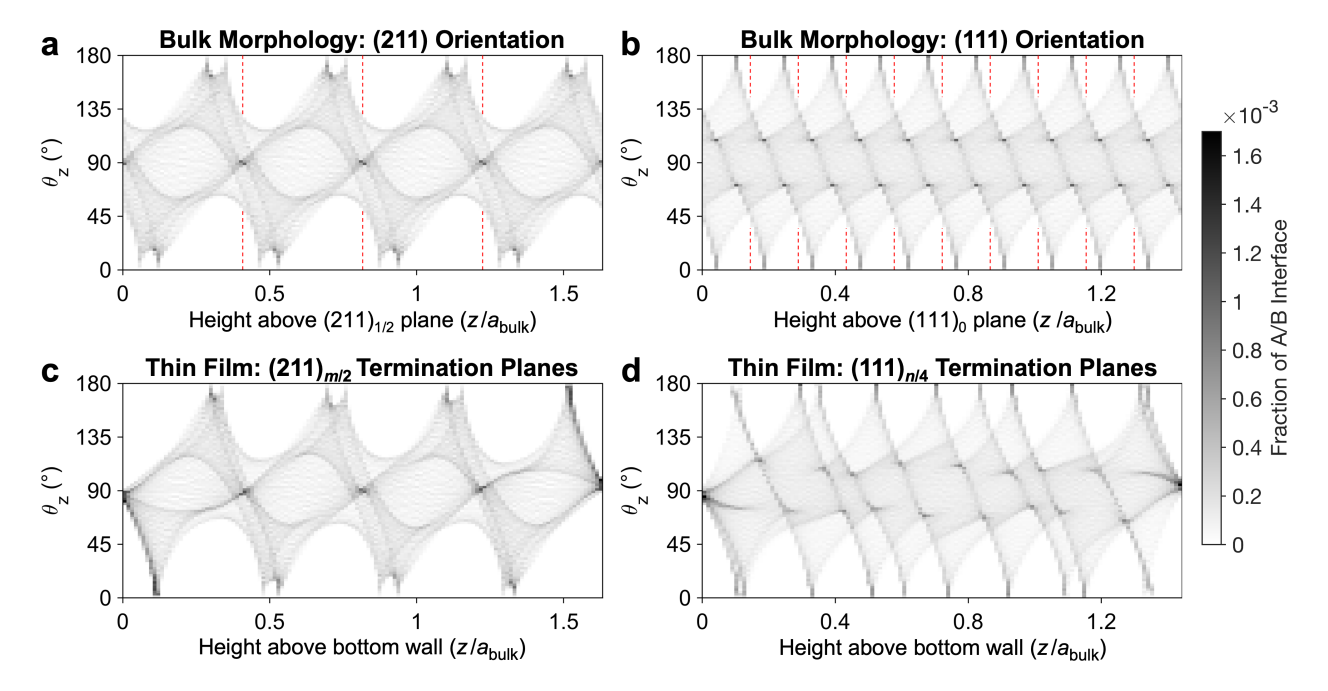


Figure 3: Two-dimensional histograms showing the angle of the A/B interface as a function of position, comparing bulk and thin-film morphologies. a) Distribution of the angle θ_z between the A/B interface and the (211) plane as a function of position in the bulk DG morphology. Panel b) shows the corresponding distribution for the (111) plane. Red dashed lines in a) and b) indicate the locations of $(211)_{m/2}$ and $(111)_{n/4}$ planes, respectively, where m is an odd integer and n is an integer. c) and d) show similar distributions for thin films with $(211)_{m/2}$ and $(111)_{n/4}$ termination planes, respectively, as a function of height in the film. In c) and d), θ_z refers to the angle between the A/B interface and the bottom wall of the film. a_{bulk} is the lattice parameter for the DG unit cell in the bulk. The angle θ_z is measured on the minority-domain side of the A/B interface.

Figures 3a and 3b show the distribution of θ_z in the bulk DG morphology in the (211) and (111) orientations, respectively. In Figure 3a, there is a $(211)_{m/2}$ plane on the leftmost

and rightmost edges of the figure, along with several interior $(211)_{m/2}$ planes indicated by red dashed lines; the same is true of $(111)_{n/4}$ planes in Figure 3b. The $(211)_{m/2}$ planes exhibit a high density of points with $\theta_z = 90^{\circ}$, while the $(111)_{n/4}$ planes in Figure 3b have a much broader θ_z distribution. Thus, it is reasonable to expect from these data alone that $(211)_{m/2}$ termination planes will accommodate the preferred wetting angle of 85° well, while $(111)_{n/4}$ planes may not.

Figures 3c and 3d show converged solutions for thin films with $(211)_{m/2}$ and $(111)_{n/4}$ termination planes, respectively, calculated using the structures in Figures 3a and 3b as initial guesses. The left and right edges of these panels correspond to the walls of the film. At both walls in both films, the distribution of angles is very tightly clustered near 90°. Both structures clearly underwent distortion to accommodate this preferred wetting angle, since Figures 3c and 3d differ noticeably from 3a and 3b. However, the distortion in the $(111)_{n/4}$ -terminated film is significantly more severe, and pervades deeper into the film than for the $(211)_{m/2}$ -terminated film. Returning to Figure 3a, we can see why: θ_z is already concentrated around 90° on the left and right edges of the figure, which is close to the value of roughly 85° observed in Figure 3c. This demonstrates why the $(211)_{m/2}$ planes in the bulk correspond to such stable termination planes in a thin film, and why other planes are relatively less stable.

This leaves two remaining questions: why is there a preferred wetting angle, and why is it 85°? One explanation is that polymers adjacent to a wall must extend parallel to the wall, and the A/B interface tends to be perpendicular to the polymers. ⁶⁰ This implies a preferred angle of 90°. However, this cannot explain why the wetting angle changes when preferential wetting is introduced, which has been shown to occur in films of lamellae and cylinders. ^{28,30,46,61–63} Another explanation is that the optimal wetting angle is determined by balancing the interfacial tensions at the A/B/wall interface, analogous to a liquid droplet on a substrate that forms a contact angle described by Young's equation. ^{64,65} An ordered block-polymer system is much more complicated than a small-molecule liquid droplet, but

it remains true that an optimal wetting angle can be calculated using only the interfacial tensions. In this explanation, the actual wetting angles vary from this optimal value due to local packing effects. Importantly, this optimal wetting angle only depends on interfacial tensions, not the polymer phase or orientation. This explanation also provides one possible reason why the optimal wetting angle is below 90° for a nonpreferential wall, rather than exactly 90° : the entropic preference for the minority block, due to its higher density of chain ends, reduces the interfacial tension between the minority block and the wall, ⁴³ reducing the optimal wetting angle. Indeed, we find that the optimal wetting angle increases to around 90° when $f_{\rm A}$ is increased to 0.5 (see Supporting Information).

To further assess these explanations, we performed additional calculations to show the effect of preferential wetting on the wetting angles. The relative stability of different phases and orientations will be affected by preferential wetting, but we focus here solely on the wetting angles and defer any discussion of the phase behavior to future work. For two termination planes, $(211)_{1/2}$ and $(001)_{1/8}$, we held $\chi_{\rm BW}N=0$ and varied $\chi_{\rm AW}N$ in small increments, which is equivalent to varying the interfacial tension between monomer A and the wall. At each $\chi_{AW}N$ value, we calculated the wetting angle distribution across the polymer/wall interface (see Supporting Information for details), and the results are shown in Figure 4. As an additional point of comparison, the wetting angle for perpendicular lamellae at $f_{\rm A}=0.36$ is also shown, which is a single value rather than a distribution because every point on the A/B/wall interface is symmetry equivalent. While the shapes of the distributions differ slightly between the two orientations (which we do not investigate here), the preferred wetting angle follows the same general trend for both orientations of DG as a function of $\chi_{AW}N$, and the trend for perpendicular lamellae agrees as well. This supports the argument that the preferred wetting angle is determined by balancing the interfacial tensions, which are independent of the phase and orientation. However, the exact interfacial tensions are not easily accessible from our SCFT solutions, so this explanation only serves as a qualitative interpretation of our results.

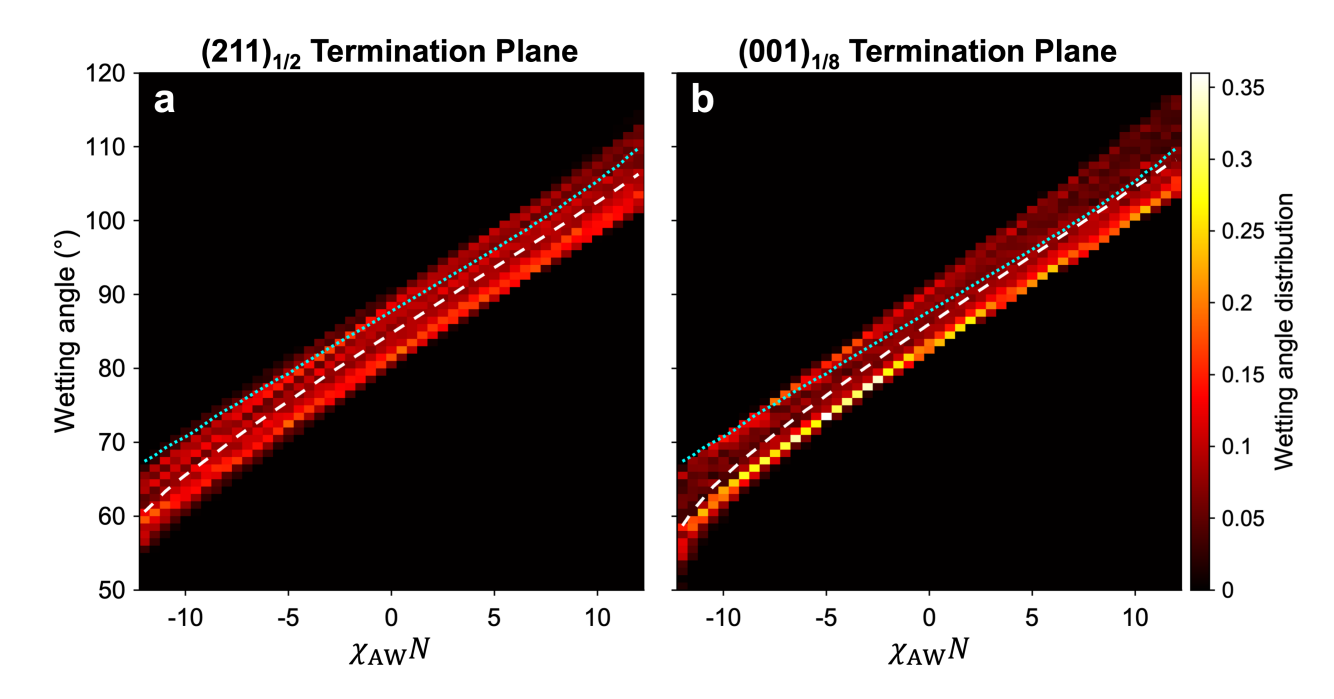


Figure 4: Distribution of wetting angles for thin films of double gyroid, shown as a function of preferential wetting ($\chi_{\rm AW}N$, where $\chi_{\rm BW}N$ is held at zero) for block polymers with $f_{\rm A}=0.36$ and $\chi N=20$. Distributions represent a) a film with $(211)_{1/2}$ termination planes, and b) a film with $(001)_{1/4}$ termination planes. The wetting angle distribution at each value of $\chi_{\rm AW}N$ is normalized to one. The average wetting angle is plotted as a dashed white line. As an additional point of reference, the wetting angle of perpendicular lamellae at $f_{\rm A}=0.36$ and $\chi N=20$ is also plotted as a cyan dotted line on both panels of the figure.

In summary, in the absence of preferential wetting, the DG termination plane that accommodates the preferred wetting angle (roughly 85°) with the least distortion relative to the bulk morphology will be the most stable termination plane, which explains why the (211)-oriented plane with the double-wave pattern is so common in DG thin films. The phenomenological model developed here in the context of a frustrated boundary also provides an explanation for observations made in very different systems; for instance, the morphology of a step edge in parallel lamellae ^{66,67} clearly exhibits the effect of a preferred wetting angle, as does the morphology and phase behavior of ultra-thin films, ^{68–70} and our results help explain why a twin boundary in DG forms on the (211)-oriented plane with the double-wave pattern. ⁵⁸

Data Availability

All data presented in this letter were generated using the open-source PSCF software, which is available at https://github.com/dmorse/pscfpp. All PSCF input and output files, as well as the scripts used to generate and process these files, will be made available at the Data Repository for U of M (https://conservancy.umn.edu/drum) at the time of publication.

Associated Content

Supporting Information

Detailed description of methods; discussion of symmetry relationships between parallel termination planes in the $Ia\overline{3}d$ space group; visualizations of SCFT initial guesses and converged solutions for each termination plane tested; an alternate version of Figure 1 with colorbars and axis ticks; an alternate version of Figure 2 showing each individual data point; a quantitative comparison of other boundary effects in various orientations of double-gyroid thin films; a description of how the wetting angle(s) of an SCFT solution were calculated; a comparison of wetting angle distributions for various phases; a description of how Figure 3 was generated.

Acknowledgement

We acknowledge conversations with Mahesh Mahanthappa, Michelle Calabrese, Emily McGuinness, Jinwoo Oh, and Szu-Ming Yang. Computational resources were provided by the Minnesota Supercomputing Institute. This work was supported primarily by the National Science Foundation through the University of Minnesota MRSEC under Award Number DMR-2011401. The software development for this project was supported by NSF award OAC-2103627.

References

- Bang, J.; Jeong, U.; Ryu, D. Y.; Russell, T. P.; Hawker, C. J. Block Copolymer Nanolithography: Translation of Molecular Level Control to Nanoscale Patterns. Adv. Mater. 2009, 21, 4769–4792.
- (2) Bates, C. M.; Maher, M. J.; Janes, D. W.; Ellison, C. J.; Willson, C. G. Block Copolymer Lithography. *Macromolecules* **2014**, *47*, 2–12.
- (3) Hamley, I. Ordering in Thin Films of Block Copolymers: Fundamentals to Potential Applications. *Prog. Polym. Sci.* **2009**, *34*, 1161–1210.
- (4) Albert, J. N.; Epps, T. H. Self-Assembly of Block Copolymer Thin Films. Materials Today 2010, 13, 24–33.
- (5) Huang, C.; Zhu, Y.; Man, X. Block Copolymer Thin Films. *Phys. Rep.* **2021**, *932*, 1–36.
- (6) Jackson, E. A.; Hillmyer, M. A. Nanoporous Membranes Derived from Block Copolymers: From Drug Delivery to Water Filtration. *ACS Nano* **2010**, *4*, 3548–3553.
- (7) Wu, D.; Xu, F.; Sun, B.; Fu, R.; He, H.; Matyjaszewski, K. Design and Preparation of Porous Polymers. *Chem. Rev.* **2012**, *112*, 3959–4015.
- (8) Hampu, N.; Werber, J. R.; Chan, W. Y.; Feinberg, E. C.; Hillmyer, M. A. Next-Generation Ultrafiltration Membranes Enabled by Block Polymers. ACS Nano 2020, 14, 16446–16471.
- (9) Radjabian, M.; Abetz, V. Advanced Porous Polymer Membranes from Self-Assembling Block Copolymers. *Prog. Polym. Sci.* **2020**, *102*, 101219.
- (10) Müller, M.; Abetz, V. Nonequilibrium Processes in Polymer Membrane Formation: Theory and Experiment. *Chem. Rev.* **2021**, *121*, 14189–14231.

- (11) Cummins, C.; Lundy, R.; Walsh, J. J.; Ponsinet, V.; Fleury, G.; Morris, M. A. Enabling Future Nanomanufacturing through Block Copolymer Self-Assembly: A Review. *Nano Today* 2020, 35, 100936.
- (12) Maldovan, M.; Urbas, A. M.; Yufa, N.; Carter, W. C.; Thomas, E. L. Photonic Properties of Bicontinuous Cubic Microphases. *Phys. Rev. B* **2002**, *65*, 165123.
- (13) Dolan, J. A.; Wilts, B. D.; Vignolini, S.; Baumberg, J. J.; Steiner, U.; Wilkinson, T. D. Optical Properties of Gyroid Structured Materials: From Photonic Crystals to Metamaterials. *Adv. Opt. Mater.* **2015**, *3*, 12–32.
- (14) Stefik, M.; Guldin, S.; Vignolini, S.; Wiesner, U.; Steiner, U. Block Copolymer Self-Assembly for Nanophotonics. *Chem. Soc. Rev.* **2015**, *44*, 5076–5091.
- (15) Crossland, E. J. W.; Kamperman, M.; Nedelcu, M.; Ducati, C.; Wiesner, U.; Smilgies, D. M.; Toombes, G. E. S.; Hillmyer, M. A.; Ludwigs, S.; Steiner, U.; Snaith, H. J. A Bicontinuous Double Gyroid Hybrid Solar Cell. Nano Lett. 2009, 9, 2807–2812.
- (16) Urade, V. N.; Wei, T.-C.; Tate, M. P.; Kowalski, J. D.; Hillhouse, H. W. Nanofabrication of Double-Gyroid Thin Films. *Chem. Mater.* **2007**, *19*, 768–777.
- (17) Alvarez-Fernandez, A.; Cummins, C.; Saba, M.; Steiner, U.; Fleury, G.; Ponsinet, V.; Guldin, S. Block Copolymer Directed Metamaterials and Metasurfaces for Novel Optical Devices. Adv. Opt. Mater. 2021, 9, 2100175.
- (18) Cote, B. M.; Lenart, W. R.; Ellison, C. J.; Ferry, V. E. Surface Structure Dependent Circular Dichroism in Single and Double Gyroid Metamaterials. Adv. Opt. Mater. 2022, 10, 2200363.
- (19) Hsueh, H.-Y.; Chen, H.-Y.; She, M.-S.; Chen, C.-K.; Ho, R.-M.; Gwo, S.; Hasegawa, H.; Thomas, E. L. Inorganic Gyroid with Exceptionally Low Refractive Index from Block Copolymer Templating. *Nano Lett.* 2010, 10, 4994–5000.

- (20) She, M.-S.; Lo, T.-Y.; Ho, R.-M. Controlled Ordering of Block Copolymer Gyroid Thin Films by Solvent Annealing. *Macromolecules* **2014**, *47*, 175–182.
- (21) Wu, Y.-H.; Lo, T.-Y.; She, M.-S.; Ho, R.-M. Morphological Evolution of Gyroid-Forming Block Copolymer Thin Films with Varying Solvent Evaporation Rate. *ACS Appl. Mater. Interfaces* **2015**, *7*, 16536–16547.
- (22) Aissou, K.; Mumtaz, M.; Portale, G.; Brochon, C.; Cloutet, E.; Fleury, G.; Hadziioannou, G. Templated Sub-100-nm-Thick Double-Gyroid Structure from Si-Containing Block Copolymer Thin Films. Small 2017, 13, 1603777.
- (23) Ryu, I. H.; Kim, Y. J.; Jung, Y. S.; Lim, J. S.; Ross, C. A.; Son, J. G. Interfacial Energy-Controlled Top Coats for Gyroid/Cylinder Phase Transitions of Polystyrene-Block -Polydimethylsiloxane Block Copolymer Thin Films. ACS Appl. Mater. Interfaces 2017, 9, 17427–17434.
- (24) Jo, S.; Jun, T.; Jeon, H. I.; Seo, S.; Kim, H.; Lee, S.; Ryu, D. Y. Optical Reflection from Unforbidden Diffraction of Block Copolymer Templated Gyroid Films. ACS Macro Lett. 2021, 10, 1609–1615.
- (25) Jung, J.; Lee, J.; Park, H.-W.; Chang, T.; Sugimori, H.; Jinnai, H. Epitaxial Phase Transition between Double Gyroid and Cylinder Phase in Diblock Copolymer Thin Film. *Macromolecules* **2014**, *47*, 8761–8767.
- (26) Yang, S.-M.; Oh, J.; Magruder, B. R.; Kim, H. J.; Dorfman, K. D.; Mahan-thappa, M. K.; Ellison, C. J. Surface Relief Terraces in Double-Gyroid-Forming Polystyrene-Block-Polylactide Thin Films. Phys. Rev. Mater. 2023, 7, 125601.
- (27) Matsen, M. W. Self-Assembly of Block Copolymers in Thin Films. Curr. Opin. Colloid Interface Sci. 1998, 3, 40–47.
- (28) Matsen, M. W. Thin Films of Block Copolymer. J. Chem. Phys. 1997, 106, 7781–7791.

- (29) Huinink, H. P.; Brokken-Zijp, J. C. M.; Van Dijk, M. A.; Sevink, G. J. A. Asymmetric Block Copolymers Confined in a Thin Film. *J. Chem. Phys.* **2000**, *112*, 2452–2462.
- (30) Geisinger, T.; Müller, M.; Binder, K. Symmetric Diblock Copolymers in Thin Films. I. Phase Stability in Self-Consistent Field Calculations and Monte Carlo Simulations. J. Chem. Phys. 1999, 111, 5241–5250.
- (31) Wang, Q.; Yan, Q.; Nealey, P. F.; De Pablo, J. J. Monte Carlo Simulations of Diblock Copolymer Thin Films Confined between Two Homogeneous Surfaces. *J. Chem. Phys.* **2000**, *112*, 450–464.
- (32) Li, W.; Liu, M.; Qiu, F.; Shi, A.-C. Phase Diagram of Diblock Copolymers Confined in Thin Films. J. Phys. Chem. B 2013, 117, 5280–5288.
- (33) Edwards, E. W.; Montague, M. F.; Solak, H. H.; Hawker, C. J.; Nealey, P. F. Precise Control over Molecular Dimensions of Block-Copolymer Domains Using the Interfacial Energy of Chemically Nanopatterned Substrates. *Adv. Mater.* **2004**, *16*, 1315–1319.
- (34) Epps, T. H.; DeLongchamp, D. M.; Fasolka, M. J.; Fischer, D. A.; Jablonski, E. L. Substrate Surface Energy Dependent Morphology and Dewetting in an ABC Triblock Copolymer Film. *Langmuir* **2007**, *23*, 3355–3362.
- (35) Bai, W.; Hannon, A. F.; Gotrik, K. W.; Choi, H. K.; Aissou, K.; Liontos, G.; Ntetsikas, K.; Alexander-Katz, A.; Avgeropoulos, A.; Ross, C. A. Thin Film Morphologies of Bulk-Gyroid Polystyrene-*Block*-Polydimethylsiloxane under Solvent Vapor Annealing.

 *Macromolecules** 2014, 47, 6000–6008.
- (36) Lee, S.; Cheng, L.-C.; Gadelrab, K. R.; Ntetsikas, K.; Moschovas, D.; Yager, K. G.; Avgeropoulos, A.; Alexander-Katz, A.; Ross, C. A. Double-Layer Morphologies from a Silicon-Containing ABA Triblock Copolymer. *ACS Nano* **2018**, *12*, 6193–6202.

- (37) Jung, J.; Park, H.-W.; Lee, S.; Lee, H.; Chang, T.; Matsunaga, K.; Jinnai, H. Effect of Film Thickness on the Phase Behaviors of Diblock Copolymer Thin Film. *ACS Nano* **2010**, 4, 3109–3116.
- (38) Henkee, C. S.; Thomas, E. L.; Fetters, L. J. The Effect of Surface Constraints on the Ordering of Block Copolymer Domains. *J. Mater. Sci.* **1988**, *23*, 1685–1694.
- (39) Coulon, G.; Russell, T. P.; Deline, V. R.; Green, P. F. Surface-Induced Orientation of Symmetric, Diblock Copolymers: A Secondary Ion Mass-Spectrometry Study. *Macro-molecules* 1989, 22, 2581–2589.
- (40) Anastasiadis, S. H.; Russell, T. P.; Satija, S. K.; Majkrzak, C. F. Neutron Reflectivity Studies of the Surface-Induced Ordering of Diblock Copolymer Films. *Phys. Rev. Lett.* 1989, 62, 1852–1855.
- (41) Huinink, H. P.; Van Dijk, M. A.; Brokken-Zijp, J. C. M.; Sevink, G. J. A. Surface-Induced Transitions in Thin Films of Asymmetric Diblock Copolymers. *Macromolecules* **2001**, *34*, 5325–5330.
- (42) Knoll, A.; Horvat, A.; Lyakhova, K. S.; Krausch, G.; Sevink, G. J. A.; Zvelindovsky, A. V.; Magerle, R. Phase Behavior in Thin Films of Cylinder-Forming Block Copolymers. Phys. Rev. Lett. 2002, 89, 035501.
- (43) Pickett, G. T.; Witten, T. A.; Nagel, S. R. Equilibrium Surface Orientation of Lamellae.

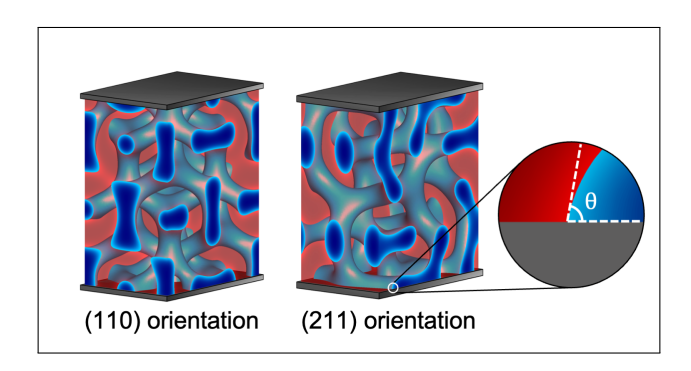
 *Macromolecules 1993, 26, 3194–3199.
- (44) Sommer, J.-U.; Hoffmann, A.; Blumen, A. Block Copolymer Films between Neutral Walls: A Monte Carlo Study. *J. Chem. Phys.* **1999**, *111*, 3728–3732.
- (45) Wang, Q.; Nealey, P. F.; De Pablo, J. J. Monte Carlo Simulations of Asymmetric Diblock Copolymer Thin Films Confined between Two Homogeneous Surfaces. *Macro-molecules* 2001, 34, 3458–3470.

- (46) Szamel, G.; Müller, M. Thin Films of Asymmetric Triblock Copolymers: A Monte Carlo Study. J. Chem. Phys. 2003, 118, 905–913.
- (47) Meng, D.; Wang, Q. Hard-Surface Effects in Polymer Self-Consistent Field Calculations.
 J. Chem. Phys. 2007, 126, 234902.
- (48) Sikka, M.; Singh, N.; Karim, A.; Bates, F. S.; Satija, S. K.; Majkrzak, C. F. Entropy-Driven Surface Segregation in Block Copolymer Melts. *Phys. Rev. Lett.* **1993**, *70*, 307–310.
- (49) Spencer, R. K. W.; Matsen, M. W. Universality of Entropic Surface Segregation from Athermal Polymer Blends Due to Conformational Asymmetry. *Macromolecules* 2022, 55, 1120–1126.
- (50) Matsen, M. W. Entropic Surface Segregation from Athermal Polymer Blends: Polymer Flexibility vs Bulkiness. J. Chem. Phys. 2022, 156, 184901.
- (51) Silberberg, A. Distribution of Conformations and Chain Ends near the Surface of a Melt of Linear Flexible Macromolecules. *J. Colloid Interface Sci.* **1982**, *90*, 86–91.
- (52) Sinturel, C.; Vayer, M.; Morris, M.; Hillmyer, M. A. Solvent Vapor Annealing of Block Polymer Thin Films. *Macromolecules* **2013**, *46*, 5399–5415.
- (53) Posselt, D.; Zhang, J.; Smilgies, D.-M.; Berezkin, A. V.; Potemkin, I. I.; Papadakis, C. M. Restructuring in Block Copolymer Thin Films: In Situ GISAXS Investigations during Solvent Vapor Annealing. *Prog. Polym. Sci.* 2017, 66, 80–115.
- (54) Fredrickson, G. H. *The Equilibrium Theory of Inhomogeneous Polymers*; Oxford University Press: Oxford, 2006.
- (55) Khanna, V.; Cochran, E. W.; Hexemer, A.; Stein, G. E.; Fredrickson, G. H.; Kramer, E. J.; Li, X.; Wang, J.; Hahn, S. F. Effect of Chain Architecture and Surface

- Energies on the Ordering Behavior of Lamellar and Cylinder Forming Block Copolymers. *Macromolecules* **2006**, *39*, 9346–9356.
- (56) Arora, A.; Qin, J.; Morse, D. C.; Delaney, K. T.; Fredrickson, G. H.; Bates, F. S.; Dorfman, K. D. Broadly Accessible Self-Consistent Field Theory for Block Polymer Materials Discovery. *Macromolecules* 2016, 49, 4675–4690.
- (57) Cheong, G. K.; Chawla, A.; Morse, D. C.; Dorfman, K. D. Open-Source Code for Self-Consistent Field Theory Calculations of Block Polymer Phase Behavior on Graphics Processing Units. Eur. Phys. J. E 2020, 43, 15.
- (58) Feng, X.; Zhuo, M.; Guo, H.; Thomas, E. L. Visualizing the Double-Gyroid Twin. *Proc. Natl. Acad. Sci. U.S.A.* **2021**, *118*, e2018977118.
- (59) Antoine, S.; Aissou, K.; Mumtaz, M.; Telitel, S.; Pécastaings, G.; Wirotius, A.-L.; Brochon, C.; Cloutet, E.; Fleury, G.; Hadziioannou, G. Core-Shell Double Gyroid Structure Formed by Linear ABC Terpolymer Thin Films. *Macromol. Rapid Commun.* 2018, 39, 1800043.
- (60) Dimitriyev, M. S.; Reddy, A.; Grason, G. M. Medial Packing, Frustration, and Competing Network Phases in Strongly Segregated Block Copolymers. *Macromolecules* 2023, 56, 7184–7202.
- (61) Geisinger, T.; Müller, M.; Binder, K. Symmetric Diblock Copolymers in Thin Films. II. Comparison of Profiles between Self-Consistent Field Calculations and Monte Carlo Simulations. J. Chem. Phys. 1999, 111, 5251–5258.
- (62) Pickett, G. T.; Balazs, A. C. Equilibrium Orientation of Confined Diblock Copolymer Films. *Macromolecules* **1997**, *30*, 3097–3103.
- (63) Angerman, H. J.; Johner, A.; Semenov, A. N. Microphase Separation in Thin Block

- Copolymer Films: A Weak Segregation Mean-Field Approach. *Macromolecules* **2006**, 39, 6210–6220.
- (64) Young, T. An Essay on the Cohesion of Fluids. Phil. Trans. R. Soc. 1805, 95, 65–87.
- (65) Berg, J. C. An Introduction to Interfaces & Colloids: The Bridge to Nanoscience; World Scientific: Singapore; Hackensack, NJ, 2010.
- (66) Stasiak, P.; McGraw, J. D.; Dalnoki-Veress, K.; Matsen, M. W. Step Edges in Thin Films of Lamellar-Forming Diblock Copolymer. *Macromolecules* **2012**, *45*, 9531–9538.
- (67) Maher, M. J.; Self, J. L.; Stasiak, P.; Blachut, G.; Ellison, C. J.; Matsen, M. W.; Bates, C. M.; Willson, C. G. Structure, Stability, and Reorganization of 0.5 L₀ Topography in Block Copolymer Thin Films. ACS Nano 2016, 10, 10152–10160.
- (68) Michman, E.; Langenberg, M.; Stenger, R.; Oded, M.; Schvartzman, M.; Müller, M.; Shenhar, R. Controlled Spacing between Nanopatterned Regions in Block Copolymer Films Obtained by Utilizing Substrate Topography for Local Film Thickness Differentiation. ACS Appl. Mater. Interfaces 2019, 11, 35247–35254.
- (69) Aviv, Y.; Altay, E.; Burg, O.; Müller, M.; Rzayev, J.; Shenhar, R. Bottlebrush Block Copolymer Assembly in Ultraconfined Films: Effect of Substrate Selectivity. *Macro-molecules* 2021, 54, 2079–2089.
- (70) Li, L.; Jia, X.; Dong, Q.; Zhou, J.; Li, W. Thickness-Controlled Phase Transitions of AB Diblock Copolymers in Asymmetric Ultrathin Films. *Macromolecules* 2023, 56, 5932–5940.

TOC Graphic



For Table of Contents Only

Supporting Information for Boundary Frustration in Double-Gyroid Thin Films

Benjamin R. Magruder, David C. Morse, Christopher J. Ellison, and Kevin D. Dorfman*

Department of Chemical Engineering and Materials Science, University of Minnesota Twin Cities, 421 Washington Avenue SE, Minneapolis, Minnesota 55455, USA

E-mail: dorfman@umn.edu

Contents

1	Methods			
	1.1	Self-consistent field theory for thin films	3	
	1.2	Calculation parameters	8	
2	Symmetry relationships of parallel termination planes			
	2.1	A more rigorous description of termination planes	10	
	2.2	Symmetry relationships in each orientation	11	
		2.2.1 (211) orientation	11	
		2.2.2 (001) orientation	11	
		2.2.3 (111) orientation	12	
		2.2.4 (110) orientation	12	
3	SCE	Tresults: Varying termination planes	14	
	3.1	Competing morphologies in the (110) orientation	19	
4	Alte	ernate version of Figure 1	21	
5	Data points used to construct Figure 2			
6	Oth	er boundary effects in double-gyroid films	23	
7	Calculating the wetting angle			
8	Wet	etting angles in other candidate phases		
9	Construction of Figure 3			
10	Wet	sting angles at $f_{ m A}=0.5$	31	
\mathbf{Re}	References 3			

1 Methods

1.1 Self-consistent field theory for thin films

All data presented in this work are calculated using the open-source PSCF software package (C++ version), which implements the standard periodic SCFT for continuous Gaussian chains, a iteratively solving for the self-consistent potential fields using Anderson Mixing with variable unit cell size. The software is available at https://github.com/dmorse/pscfpp. For this project, we added a new feature into the software that allows users to impose a mask and an external field of arbitrary geometry into the iterative algorithm, a technique first described by Matsen. This new feature in PSCF was validated by successfully reproducing Matsen's results for lamellar thin films confined between preferential walls.

The relevant equations for our SCFT calculations are described briefly here for the case of a neat melt of conformationally symmetric AB diblock polymers under thin film confinement studied in the main text. We define the polymer system within a unit cell of arbitrary size/shape and periodic boundary conditions in all directions, with a total volume V. The AB diblock polymer has total degree of polymerization N, statistical segment length b (which we define to be the same for both A and B), and a composition defined by the volume fraction species A, $f = N_A/N$. In the mean field approximation, each monomer species (A or B) has an effective chemical potential field defined by

$$w_{\rm A}(\mathbf{r}) = \chi \phi_{\rm B}(\mathbf{r}) + w_{\rm A,ext} + \xi(\mathbf{r})$$

$$w_{\rm B}(\mathbf{r}) = \chi \phi_{\rm A}(\mathbf{r}) + w_{\rm B,ext} + \xi(\mathbf{r}) ,$$
(1)

where χ is the effective Flory–Huggins interaction parameter between species A and B, $\phi_{\alpha}(\mathbf{r})$ is the volume fraction of species α at position \mathbf{r} , and $w_{\alpha,ext}$ is an external potential field felt by species α at position \mathbf{r} . These external fields can assume any arbitrary shape, defined as an optional input to the SCFT calculation. $\xi(\mathbf{r})$ is a Lagrange multiplier field that is used

to enforce the incompressibility constraint

$$\phi_{\mathcal{A}}(\mathbf{r}) + \phi_{\mathcal{B}}(\mathbf{r}) = \phi_m(\mathbf{r}) , \qquad (2)$$

where ϕ_m is a "mask" function that defines which regions of the unit cell can be occupied by polymeric species. For a bulk, unconfined system, $\phi_m(\mathbf{r}) = 1$ everywhere. In a confined system, the mask function takes values from 0 to 1 depending on \mathbf{r} , specifying the type of confinement imposed upon the system. When $\phi_m(\mathbf{r}) \approx 1$, \mathbf{r} is in the polymer melt, while $\phi_m(\mathbf{r}) \approx 0$ indicates that polymers cannot occupy position \mathbf{r} . We refer to this confining region where $\phi_m(\mathbf{r}) \approx 0$ as the "wall." The wall and the polymer melt are typically separated by a thin transition region at the boundary of the melt, where $\phi_m(\mathbf{r})$ drops from 1 to 0.^{5,6}

In this study, we use a narrow, sigmoid-shaped interfacial region to represent the transition between the melt and the walls. More specifically, we define the mask using the functional form described by Khanna, et al.⁷ This function describes walls oriented normal to the z-direction, with total width T, interfacial width t between the melt and the walls, and with a unit cell size of L in the z-direction:

$$\phi_m(z) = 1 - 0.5 \left(1 + \tanh \left(\frac{0.5(T - L) + |z - \frac{L}{2}|}{0.25t} \right) \right) . \tag{3}$$

An example of $\phi_m(z)$ is plotted in Figure S1 to demonstrate the shape of the function. We note here that regardless of ϕ_m , the boundary conditions remain periodic in all dimensions; the mask defined in Equation 3 merely prohibits the polymer melt from occupying the region at the very top and very bottom of the unit cell, equivalent to confinement within a thin film. The periodic boundary conditions in all dimensions allow us to solve the SCFT equations using spectral methods, taking advantage of their remarkable convergence properties.⁸

The continuous Gaussian chain model represents the configuration of the polymer as a

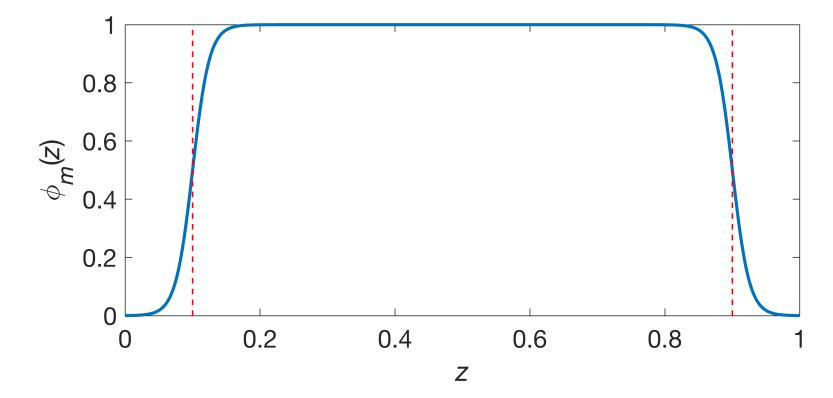


Figure S1: The function $\phi_m(z)$, shown for the case in which T = 0.2, t = 0.1, and L = 1. The red dashed lines indicate the midpoints of the polymer/wall interfaces, showing that the distance L - T between the walls is equal to 0.8.

random walk in an external field, described by the modified diffusion equations: 2,3

$$\frac{\partial q(\mathbf{r}, s)}{\partial s} = \left[\frac{b^2}{6} \nabla^2 - w_{\alpha(s)}(\mathbf{r}) \right] q(\mathbf{r}, s)
- \frac{\partial q^{\dagger}(\mathbf{r}, s)}{\partial s} = \left[\frac{b^2}{6} \nabla^2 - w_{\alpha(s)}(\mathbf{r}) \right] q^{\dagger}(\mathbf{r}, s) ,$$
(4)

where s spans from 0 to N and represents the position along the contour of the polymer, and $\alpha(s) = A$ or B depending on whether s points to an A segment or B segment. $q(\mathbf{r}, s)$ is a constrained partition function (also called a "propagator") for the segment of chain between 0 and s, under the constraint that contour position s on the polymer is pinned at position \mathbf{r} . $q^{\dagger}(\mathbf{r}, s)$ is a complementary propagator for the remaining section of the diblock, between s and N. We solve both constrained partition functions numerically using a pseudospectral method 2,3,9,10 starting from an initial condition of $q(\mathbf{r}, 0) = q^{\dagger}(\mathbf{r}, N) = 1$.

From the propagators, we can calculate the total partition function

$$Q = \frac{1}{\overline{\phi}_m V} \int d\mathbf{r} \, q(\mathbf{r}, N) , \qquad (5)$$

where $\overline{\phi}_m$ is the average value of $\phi_m(\mathbf{r})$ over the entire unit cell, i.e., the fraction of the unit cell occupied by polymers. The quantity $\overline{\phi}_m V$ represents the volume of space that is accessible to the polymers. Although the spatial integrals used here and in what follows are

calculated over the entire unit cell volume V, the integrals are normalized by the volume $\overline{\phi}_m V$ because that is the volume that is relevant to the polymer system. This can be understood in the context of the mask function ϕ_m in Equation 3: for a film with thickness L-T, the partition function Q must be invariant to changes in the wall thickness T, because the wall thickness can be made arbitrarily large without affecting the polymers.

We can then calculate the composition (volume fraction) field for each species

$$\phi_{A}(\mathbf{r}) = \frac{1}{NQ} \int_{0}^{fN} ds \, q(\mathbf{r}, s) q^{\dagger}(\mathbf{r}, s)$$

$$\phi_{B}(\mathbf{r}) = \frac{1}{NQ} \int_{fN}^{N} ds \, q(\mathbf{r}, s) q^{\dagger}(\mathbf{r}, s) .$$
(6)

Altogether, Equations 1-6 fully describe the polymer system. The final step is to algorithmically identify a set of fields w_A and w_B that satisfy all of the above equations simultaneously, to represent a thermodynamically valid candidate phase in the mean field approximation. For this, we start from a set of initial guess fields and converge to the solution use the Anderson Mixing algorithm with variable unit cell size, 4 modified such that the unit cell cannot change size along the z-direction normal to the walls (i.e., the film thickness is held fixed while the other lattice parameters can relax to optimal values).

Different initial guesses result in convergence to different phases; the phase that is globally stable for a given polymer system can be determined by comparing the free energy of all candidate phases.³ To construct initial guesses for the potential fields, we began with a guess for the composition profile of each species. We then converted these composition profiles to potential fields using a modified version of Equation 1 in which we approximate $\xi(\mathbf{r})$ to be zero everywhere:³

$$w_{\text{A,guess}}(\mathbf{r}) = \chi \phi_{\text{B,guess}}(\mathbf{r}) + w_{\text{A,ext}}$$

$$w_{\text{B,guess}}(\mathbf{r}) = \chi \phi_{\text{A,guess}}(\mathbf{r}) + w_{\text{B,ext}}.$$
(7)

The approximation in which we neglect $\xi(\mathbf{r})$ when constructing the initial guess potential

fields does not generally hinder our ability to reach a converged solution.

For a converged solution, the Helmholtz free energy per chain is calculated by ⁷

$$\frac{F}{nk_{\rm B}T} = -\frac{1}{N}\ln\left(Qe\right) + \frac{1}{\overline{\phi}_{m}V} \left\{ \chi \int d\mathbf{r} \,\phi_{\rm A}(\mathbf{r})\phi_{\rm B}(\mathbf{r}) - \int d\mathbf{r} \left[w_{\rm A}(\mathbf{r}) - w_{\rm A,ext}(\mathbf{r})\right]\phi_{\rm A}(\mathbf{r}) - \int d\mathbf{r} \left[w_{\rm B}(\mathbf{r}) - w_{\rm B,ext}(\mathbf{r})\right]\phi_{\rm B}(\mathbf{r}) \right\} , \tag{8}$$

where, as in Equation 5, the unit cell integrals are normalized by $\overline{\phi}_m V$, the volume available to the polymer.

The last important detail of our implementation is the choice of external fields $w_{A,ext}$ and $w_{B,ext}$ in Equation 1. In this study, we use these fields to mimic the effects of preferential wetting, which arises as a result of each monomer species having a unique interfacial tension with the walls. This tension is manifest as a so-called "surface field" that is felt only by polymers at or near the polymer-wall interface.⁵

Here, we choose to implement our surface fields so that the wall/polymer interactions operate analogously to the polymer/polymer interactions.⁷ Specifically, the energetic contribution from A/B interactions is proportional to $\chi \int d\mathbf{r} \phi_{\rm A} \phi_{\rm B}$, the overlap integral of the two species times a Flory-Huggins χ parameter. We set $w_{\alpha,ext} = \chi_{\alpha\rm W}(1-\phi_m)$, where $\alpha = A$ or B and $\chi_{\alpha\rm W}$ is a Flory-Huggins-like interaction parameter between species α and the wall, so that the energetic contribution from wall/polymer interactions is proportional to $\chi_{\alpha\rm W} \int d\mathbf{r} \phi_{\alpha}(1-\phi_m)$. Note that $(1-\phi_m)$ is the volume fraction of the wall.

In a binary AB system, we expect that the difference in interfacial tension is the central parameter driving phase behavior, rather than the absolute magnitudes of the interfacial tensions;⁵ thus, in theory we could simplify the problem of preferential wetting down to a single external field rather than two. However, our PSCF software is generalized to solve the SCFT equations for systems with any number of monomer species, so we implement the external fields as independent entities tied to each monomer species for maximum customizability. We also implemented the ability for the top wall to have a different $\chi_{\alpha W}$ parameter than the bottom wall, though all of the polymer systems studied herein have chemically

identical walls.

1.2 Calculation parameters

For all calculations in this study, we set the segregation strength $\chi N=20$, placing the systems in the intermediate segregation regime. For simplicity, we model a conformationally symmetric diblock polymer, for which the statistical segment lengths $b_{\rm A}$ and $b_{\rm B}$ are equal. At this value of χN in a conformationally symmetric system, DG is stable in the bulk in only a narrow composition window centered at f=0.36, which we use as our A-block fraction. We hold $\chi_{\rm BW}=0$ and vary $\chi_{\rm AW}$ to model the effect of preferential wetting.

We use a polymer/wall interface thickness $t = 0.2N^{1/2}b$, or roughly $R_g/2$ (where R_g is the polymer's unperturbed radius of gyration), and a wall thickness $T = 0.4N^{1/2}b$. In agreement with a previous study,⁷ our tests indicate that this value of t is sufficiently small to capture all of the important behavior, and further reductions in t produce qualitatively identical results while requiring prohibitively high resolutions.

The resolutions of our calculations are chosen such that the resulting free energies are accurate to within $\pm 5 \times 10^{-4} k_{\rm B}T$ per chain. Our tests indicate that this level of accuracy requires high resolution in the direction normal to the wall. More specifically, the spacing between gridpoints in this direction should be at least five times smaller than the interfacial width t. Otherwise, the resolution is not high enough to accurately resolve the details of the polymer/wall interface. This is about double the required resolution along dimensions parallel to the walls. Similarly, when solving Equation 4 using the pseudospectral method, a small value of the chain discretization parameter ds is required to resolve the polymer/wall interface. We find that $ds \leq t/40$ is sufficient to get accurate results, so we use $ds = 0.005N^{1/2}b$ here. In the Anderson mixing algorithm used to iterate to a self-consistent solution, we use between 50 and 100 histories, and use an error threshold of 1×10^{-6} , which is sufficient to achieve our desired accuracy. As representative examples, the resolutions used for the four films in Figure 1 of the main text are given in Table S1.

Table S1: Film thicknesses and resolutions for the four thin films shown in Figure 1 of the main text.

Termination plane	Film thickness/ $(N^{1/2}b)$	Number of gridpoints
$(211)_{1/2}$	6.85	$92 \times 56 \times 276$
$(001)_{1/8}$	5.35	$64 \times 64 \times 176$
$(111)_0$	7.20	$96 \times 96 \times 308$
$(110)_{1/4}$	5.95	$96 \times 64 \times 208$

2 Symmetry relationships of parallel termination planes

As mentioned in the main text, the full set of symmetry-equivalent, stable termination planes in each orientation is $(211)_{m/2}$, $(001)_{m/8}$, $(111)_{n/4}$, and $(110)_{m/4}$, where m is any odd integer and n is any integer. This is true specifically for the $Ia\overline{3}d$ space group. Below, we derive each of these relationships for this space group.

2.1 A more rigorous description of termination planes

Before going into the details, it is necessary to clarify exactly what constitutes a symmetry-equivalent termination plane. Importantly, a single plane can represent two different termination planes, depending on which side of the plane represents the wall and which side of the plane contains polymer. Two planes may be related by a space-group symmetry operation but not be equivalent termination planes. Thus, for our purposes, two parallel planes are considered symmetry-equivalent termination planes if the polymer domains above the two planes have an identical morphology and the polymer domains below the two planes have an identical morphology. The two planes may differ relative to one another by any symmetry operations that do not affect the structure, such as an in-plane translation, in-plane rotation, or reflection by a mirror that is perpendicular to the plane. Two termination planes are not symmetry-equivalent if the polymer domains above one plane match the polymer domains below the other plane, and vice versa; in other words, if two planes are identical but for a mirror reflection parallel to the plane, or if they are identical but for an inversion about an inversion center, then they are not symmetry-equivalent termination planes.

For the notation used in this letter, we use the termination plane of the *upper* boundary of the film to define the termination plane being studied. The plane at the upper boundary of the film, $(hkl)_{\tau}$, is defined relative to the origin as described in the main text, and the wall is always located on the side of the plane that does *not* contain the origin. The bottom boundary of the thin film has a termination plane defined by $(hkl)_{-\tau}$, with the wall

again positioned on the side of the plane that does not contain the origin. This allows the morphology to be the same on the top and bottom boundaries of the film. This equivalence relies on the fact that DG has an inversion center at its origin, and is not generalizable to all structures.

2.2 Symmetry relationships in each orientation

Before discussing each orientation individually, we note that, by definition, the termination plane $(hkl)_{\tau}$ is equivalent by symmetry to the termination plane $(hkl)_{\tau+1}$ for any value of τ by a translation along a vector on the simple cubic Bravais lattice. For example, the translation (0,0,1) in reduced coordinates will translate $(211)_{\tau}$ to $(211)_{\tau+1}$, $(001)_{\tau}$ to $(001)_{\tau+1}$, and $(111)_{\tau}$ to $(111)_{\tau+1}$. The translation (1,0,0) in reduced coordinates will translate $(110)_{\tau}$ to $(110)_{\tau+1}$.

2.2.1 (211) orientation

In the (211) orientation, the symmetry-equivalent termination planes are denoted $(211)_{m/2}$, where m is an odd integer. The symmetry operation connecting these termination planes is the operation that transforms $(211)_{\tau}$ to $(211)_{\tau+1}$. These termination planes are equivalent by symmetry regardless of space group, because these two planes are related through a translation along a vector on the simple cubic Bravais lattice as described above.

2.2.2 (001) orientation

In the (001) orientation, the symmetry-equivalent termination planes are denoted $(001)_{m/8}$, where m is an odd integer. The symmetry operation connecting these termination planes is the operation that transforms $(001)_{\tau}$ to $(001)_{\tau+(1/4)}$. These termination planes are symmetry-equivalent as a result of the 4_1 screw axis that is parallel to the [001] direction in the $Ia\overline{3}d$ space group.

2.2.3 (111) orientation

In the (111) orientation, the symmetry-equivalent termination planes are denoted $(111)_{n/4}$, where n is an integer. The symmetry operation connecting these termination planes is the operation that transforms $(111)_{\tau}$ to $(111)_{\tau+(1/4)}$. This symmetry relationship requires a somewhat more complicated discussion of the $Ia\overline{3}d$ space group. By definition, the termination planes $(111)_0$ and $(111)_1$ are related by translational symmetry because they contain lattice points on the simple cubic Bravais lattice. However, $Ia\overline{3}d$ is a body-centered space group, and the $(111)_{0.5}$ plane contains the body centers, meaning that it is also related to $(111)_0$ and $(111)_1$ by translational symmetry alone.

The $(111)_{0.25}$ and $(111)_{0.75}$ termination planes are related to the others through the dglide plane of the space group. Using reduced coordinates (x, y, z), this d-glide plane is a
reflection about the plane x = y, followed by a translation of 1/4 along the body diagonal.

Thus, (x, y, z) becomes (y + 1/4, x + 1/4, z + 1/4). By comparison, we note that d_{111} , the
shortest distance between the $(111)_0$ and $(111)_1$ planes, corresponds to a translation of 1/3along the body diagonal.

Applying this glide operation to the $(111)_0$ plane, the plane is first reflected about x = y. This simply mirrors the $(111)_0$ plane, since the plane of reflection is perpendicular to $(111)_0$, so the symmetry-equivalence is not broken. Then the plane is translated by 1/4 along the body diagonal, which shifts it to the $(111)_{0.75}$ plane. Thus, the $(111)_0$ and $(111)_{0.75}$ termination planes are related by symmetry, differing only by a reflection about x = y, making them symmetry-equivalent. By this same argument, $(111)_{0.25}$ and $(111)_1$ are related by the same symmetry operation. Using only translational symmetry and the d-glide plane, the termination planes $(111)_{n/4}$ are therefore shown to be symmetry-equivalent.

2.2.4 (110) orientation

In the (110) orientation, the symmetry-equivalent termination planes are denoted $(110)_{m/4}$, where m is an odd integer. The symmetry operation connecting these termination planes

is the operation that transforms $(110)_{\tau}$ to $(110)_{\tau+(1/2)}$. This symmetry relationship is also related to the d-glide plane described above. The x=y reflection plane is perpendicular to the plane $(110)_{\tau}$. This is followed by a translation by 1/4 of a unit cell along the body diagonal, which moves the $(110)_{\tau}$ plane to the $(110)_{\tau+(1/2)}$ position. Therefore, $(110)_{\tau}$ and $(110)_{\tau+(1/2)}$ are symmetry-equivalent termination planes, related to one another by a d-glide operation.

3 SCFT results: Varying termination planes

As described in the main text, we generated initial guesses for the following sets of termination planes: $(211)_{n/8}$, $(110)_{n/16}$, $(111)_{n/16}$, and $(001)_{n/32}$, where n = 0, 1, 2, ..., 8. The initial guesses were constructed such that their composition profiles are identical to the bulk DG morphology, with confining walls placed at the desired termination planes. This required rotation, duplication, and/or interpolation of the composition profiles of the bulk DG morphology, depending on the orientation and film thickness. In all initial guesses and converged solutions, the top and bottom termination planes have identical morphologies; in other words, they meet the criteria described in Section 2.1 above. This was enforced using space-group symmetry, in which all calculations have a symmetry operation (either inversion or rotation) that relates the top boundary of the film to the bottom boundary.

Below, we show images of the initial guesses and converged solutions for all of these calculations. As in Figure 1 of the main text, the unit cell outline is shown, which contains the walls of the film. The transparent region at the top and bottom of each image is the space occupied by the walls in the SCFT calculation.

Note that, for the (211)-oriented films in Figure S2, we begin at $\tau=1/2$ simply for convenience. In this figure, τ jumps from 7/8 to 0 as thickness increases because $\tau=0$ is symmetry-equivalent to $\tau=1$ by definition, and we only use values of τ in the range [0,1). Similarly, for the (110)-oriented films in Figure S5, we start at $\tau=1/4$ for convenience; in this case, $\tau=0$ is symmetry-equivalent to $\tau=1/2$ due to space-group symmetry, so τ jumps from 7/16 to 0 as thickness increases.

Also note that, in one case — the $(211)_{1/8}$ termination plane — the calculation did not converge, so we retried the calculation with a 5% increase in the film thickness, which then resulted in convergence. All other calculations converged using a film thickness that was commensurate with the bulk domain spacing.

Some nuances regarding the calculations in the (110) orientation are discussed in a subsection below, following the corresponding figure.

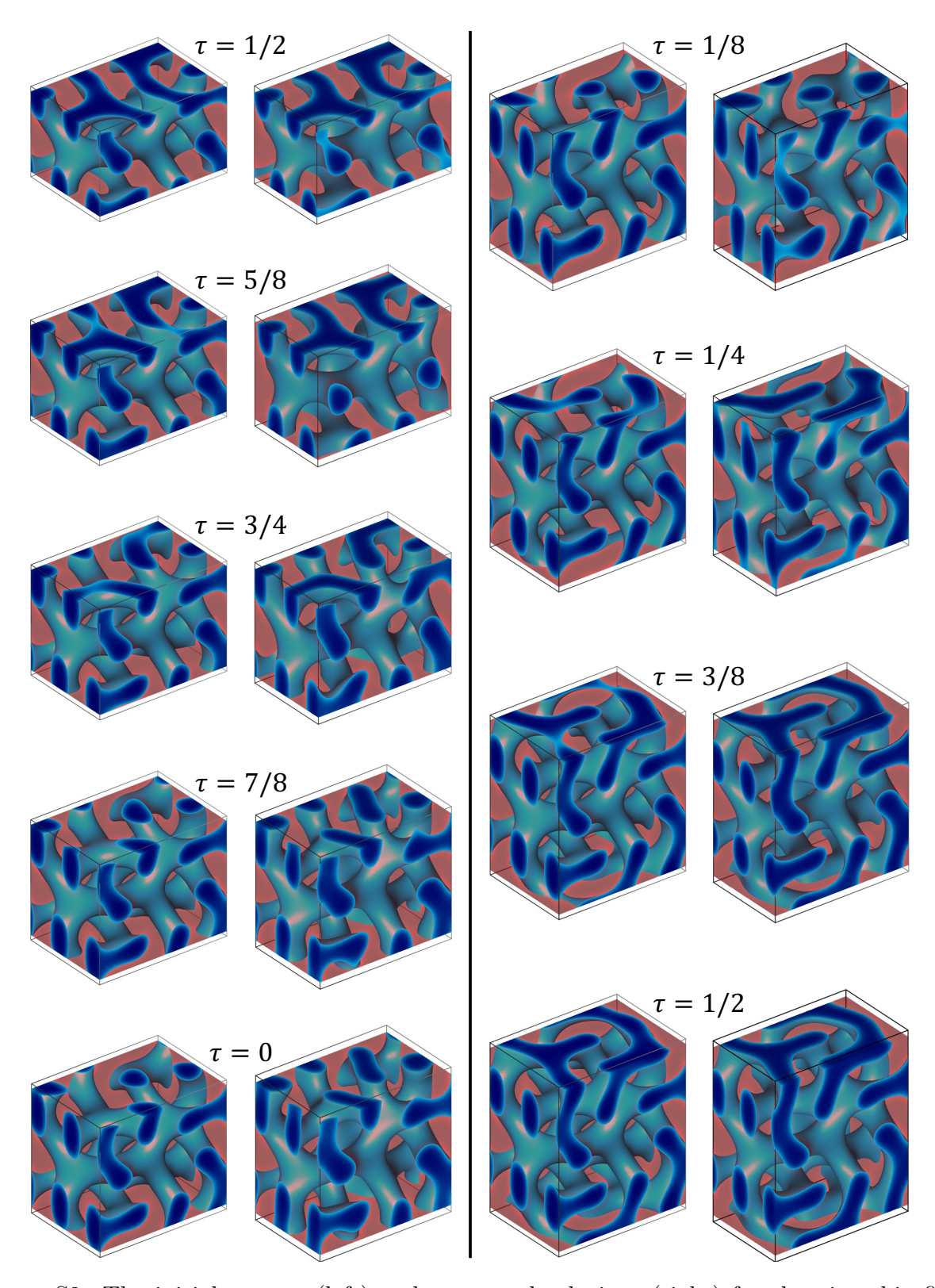


Figure S2: The initial guesses (left) and converged solutions (right) for the nine thin-film SCFT calculations performed for the (211) orientation. The termination plane of each initial guess is $(211)_{\tau}$, where τ is indicated on the figure for each initial guess.

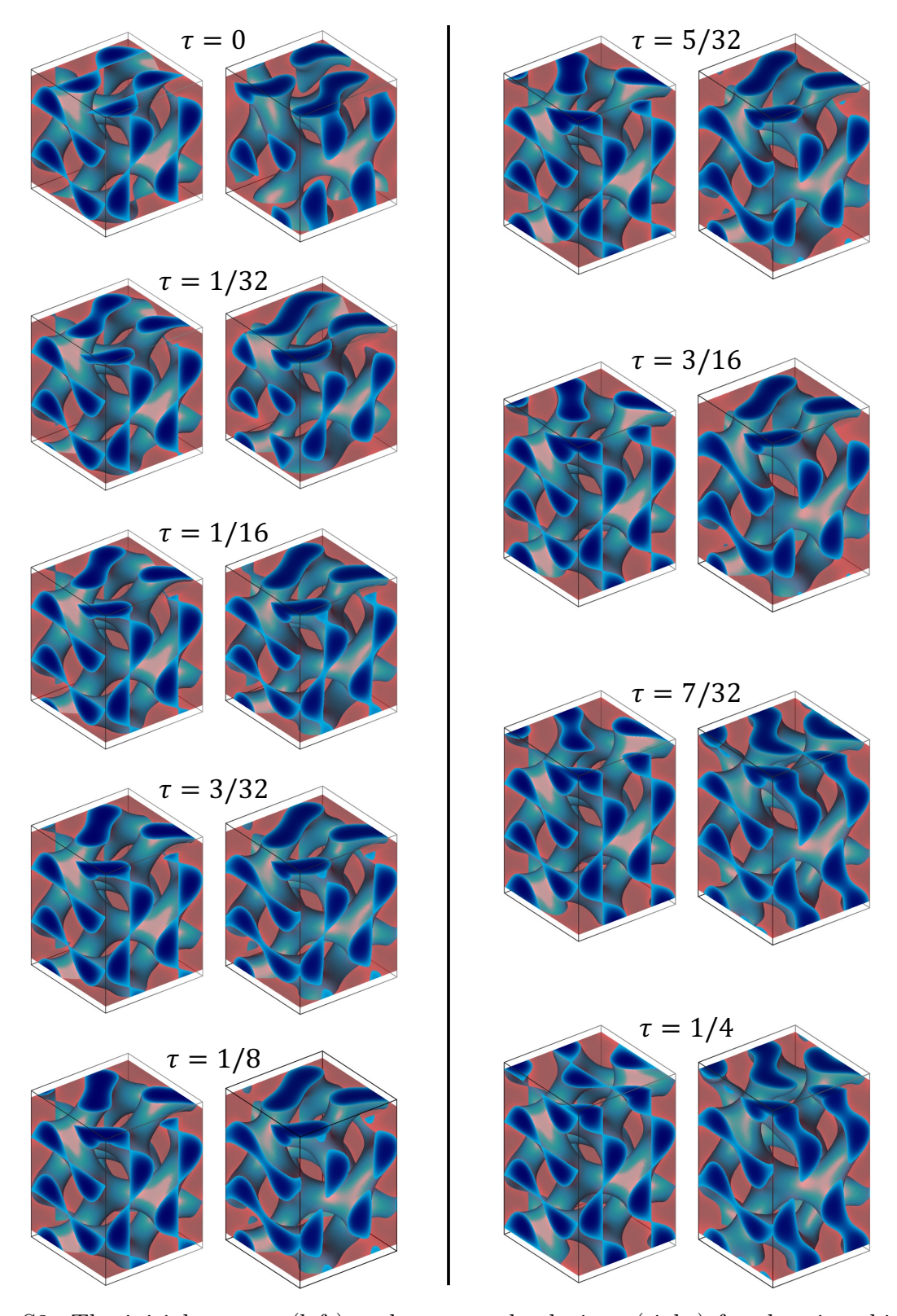


Figure S3: The initial guesses (left) and converged solutions (right) for the nine thin-film SCFT calculations performed for the (001) orientation. The termination plane of each initial guess is $(001)_{\tau}$, where τ is indicated on the figure for each initial guess.

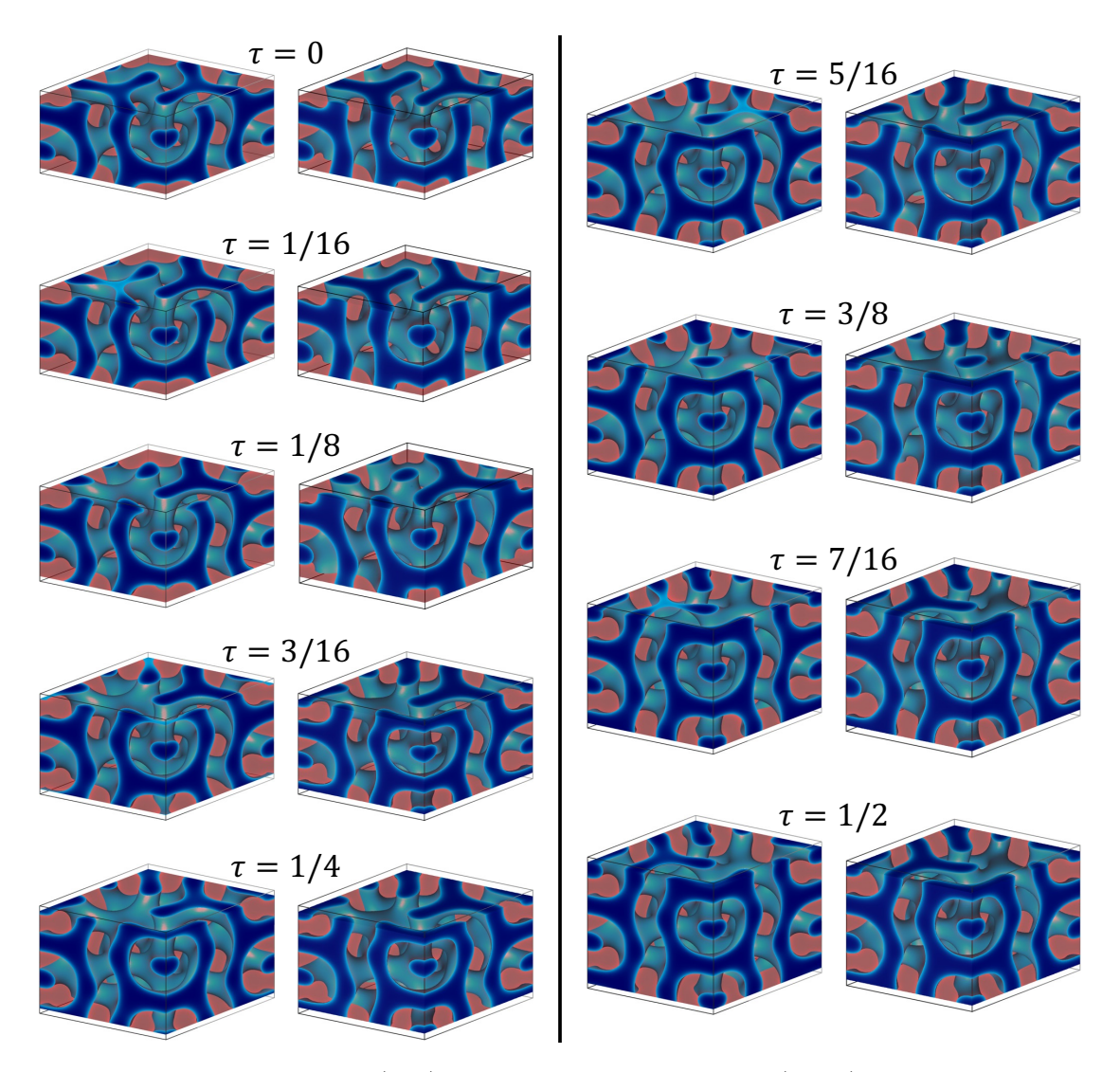


Figure S4: The initial guesses (left) and converged solutions (right) for the nine thin-film SCFT calculations performed for the (111) orientation. The termination plane of each initial guess is $(111)_{\tau}$, where τ is indicated on the figure for each initial guess.

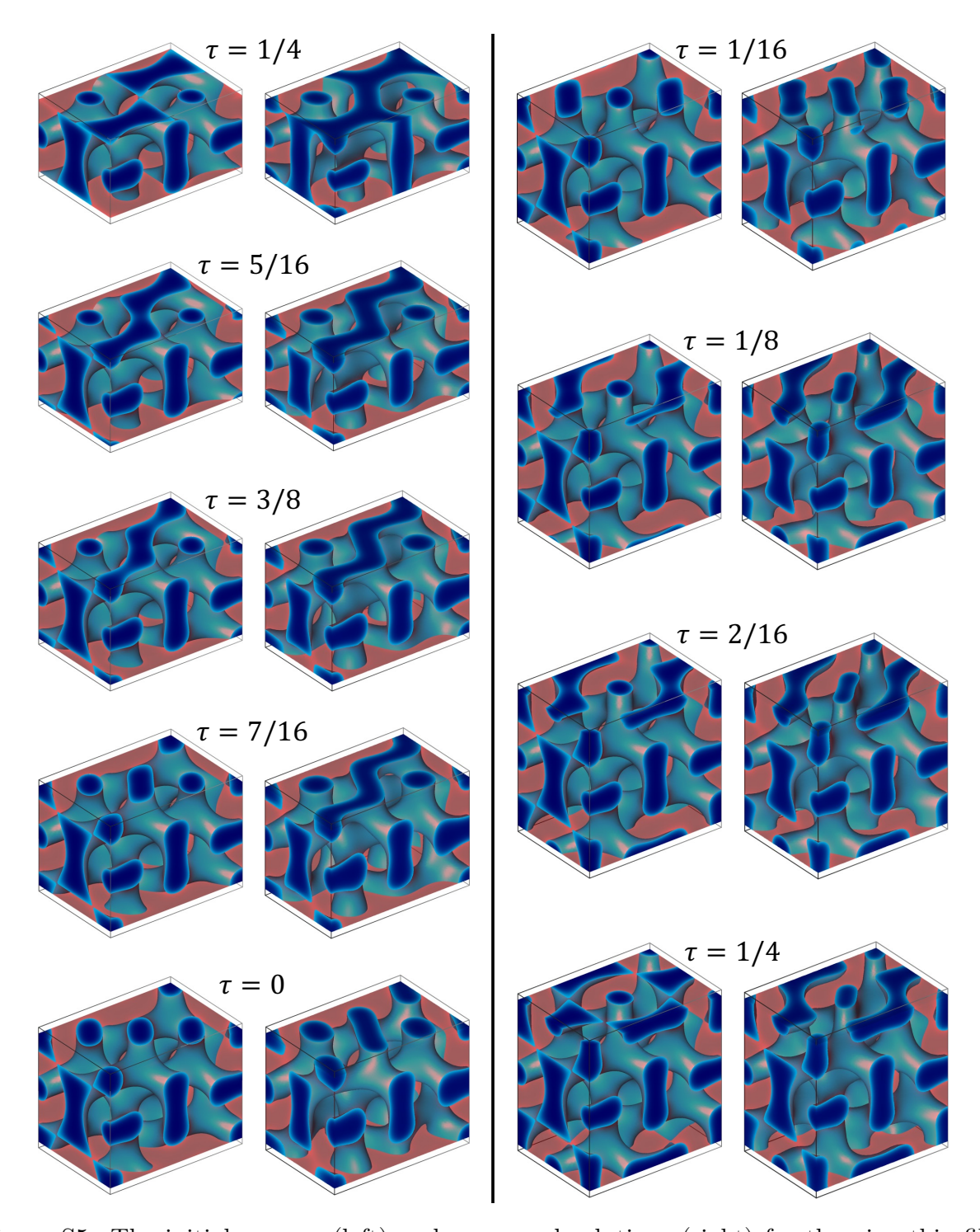


Figure S5: The initial guesses (left) and converged solutions (right) for the nine thin-film SCFT calculations performed for the (110) orientation. The termination plane of each initial guess is $(110)_{\tau}$, where τ is indicated on the figure for each initial guess.

3.1 Competing morphologies in the (110) orientation

In Figure 1 of the main text, we show the converged solution for a $(110)_{1/4}$ -terminated film, and we state that this is the most stable SCFT solution in the (110) orientation. The top surface of this SCFT solution exhibits a donut-like pattern, which has been observed experimentally. 11 However, as can be seen in Figure S5, the donut-like pattern that we show in Figure 1 of the main text only appears once in our SCFT calculations, in the $\tau = 1/4$ calculation at low thickness. A similar surface pattern appears more frequently in our calculation results, as exemplified by the SCFT solution for $\tau = 3/8$, where the blue (A-block) domain pattern is composed of dots separated by a squiggly line. Alternatively, this surface pattern can be described as a modified version of the donut-like pattern, but with neighboring donuts touching one another along one direction. This surface pattern appears for the calculations at $\tau = 5/16$, 3/8, and 7/16, and a slightly distorted version appears for the calculations at $\tau = 1/8, 2/16,$ and 1/4 at higher thickness. This "connecteddonut" pattern has been observed in thin films of ABC triblock terpolymers with a core-shell double-gyroid morphology. 12 Because this pattern is so common in our results, and the more stable pattern reported in the main text is relatively less common, it is worth going into a bit more detail here about these results.

Energetically, these two (110)-oriented morphologies are almost degenerate. At their optimal film thicknesses, the difference in excess free energy per polymer per unit area between the two morphologies is a mere $0.001k_{\rm B}T$. However, they are both quite unstable relative to the other three orientations tested, as shown in Figure 2 of the main text. This can be attributed to a high degree of boundary frustration. By comparing the initial guesses to their corresponding solutions in Figure S5, it is quite evident that the bulk gyroid morphology (seen in the initial guesses) had to undergo significant distortions to accommodate the film boundary in all 9 calculations. Contrastingly, the initial guess and converged solution for the double-wave pattern in the (211) orientation (Figure S2, $\tau = 1/2$) are nearly indistinguishable.

Because the initial guesses and converged solutions are so different, and because the two different (110)-oriented morphologies described above are nearly degenerate, it is unsurprising that our calculations fail to identify the donut-like pattern even in cases when it is thermodynamically preferred (like the $\tau=1/2$ calculation at high thickness shown in Figure S5). The iterative algorithm we use to solve the SCFT equations searches for a structure that occupies a local free-energy minimum, and these two morphologies represent separate minima in the free-energy landscape that are both quite far from the initial guess. In cases like these, there is no easy way to predict which minimum will be identified by the algorithm, and our results imply that the donut-like pattern is somewhat less likely to be found. This is merely a numerical challenge, and has no bearing on the relative stability of these morphologies or their likelihood to be observed experimentally.

Because the donut-like pattern is slightly more stable than the connected-donut pattern, we presented the donut-like pattern in the main text as the preferred morphology in the (110) orientation. Although the donut-like pattern was not observed for the thicker films in Figure S5, we managed to obtain SCFT solutions for the donut-like pattern in thicker films by constructing alternative, non-bulk-like initial guesses that already had the donut-like pattern near their boundaries. These solutions were then used for Figures 1 and 2 in the main text.

4 Alternate version of Figure 1

Below, we give an alternate version of Figure 1, in which axis ticks are included to show the size of each unit cell, and colorbars are shown in order to connect the colors to quantitative values.

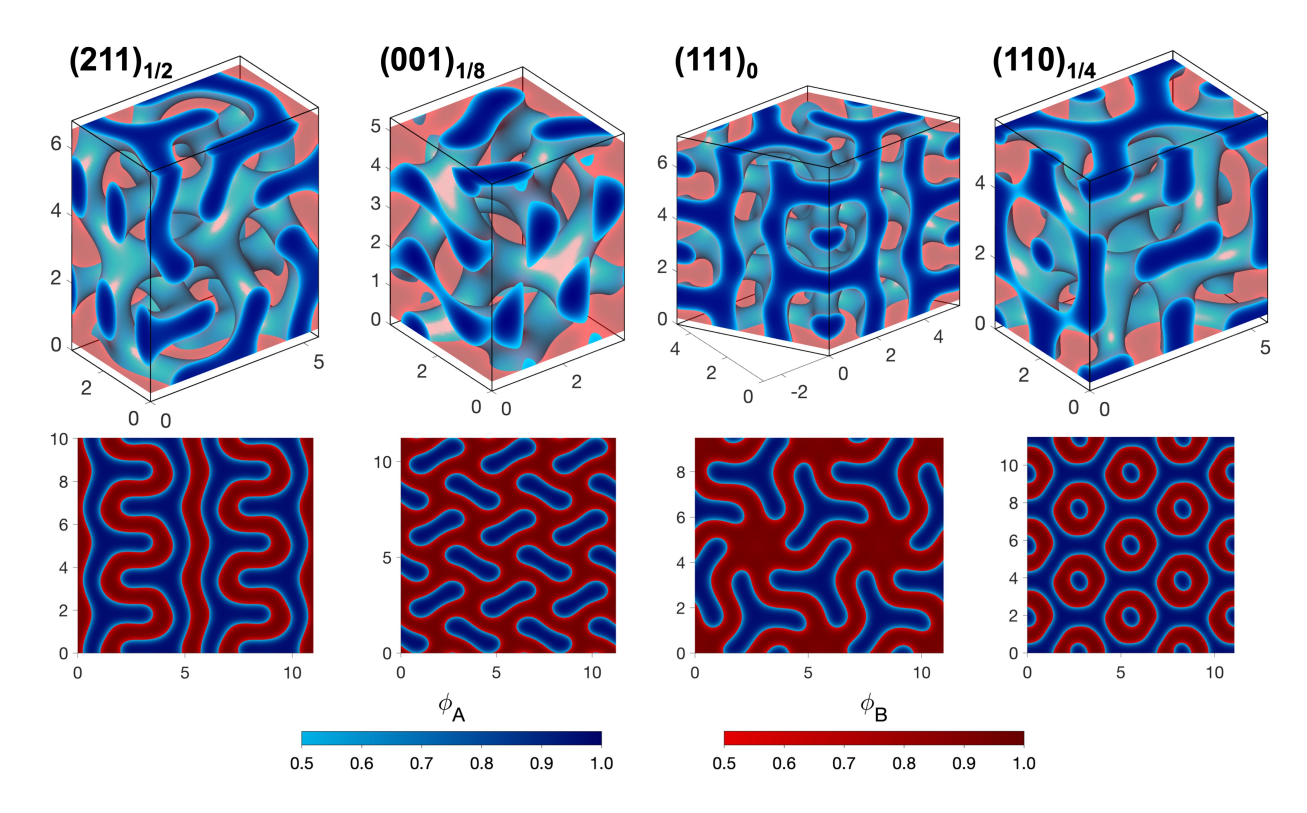


Figure S6: Identical to Figure 1 in the main text, but with tick marks, tick labels, and colorbars. All length measurements given in the figure are normalized by $N^{1/2}b$. Note that the colorbars apply only to the bottom row of images; the top row of images have been brightened and contain lighting/shading effects that alter the colors.

5 Data points used to construct Figure 2

Below, we give an alternate version of Figure 2 in which each individual SCFT calculation is shown as a dot, in order to demonstrate how the figure was constructed.

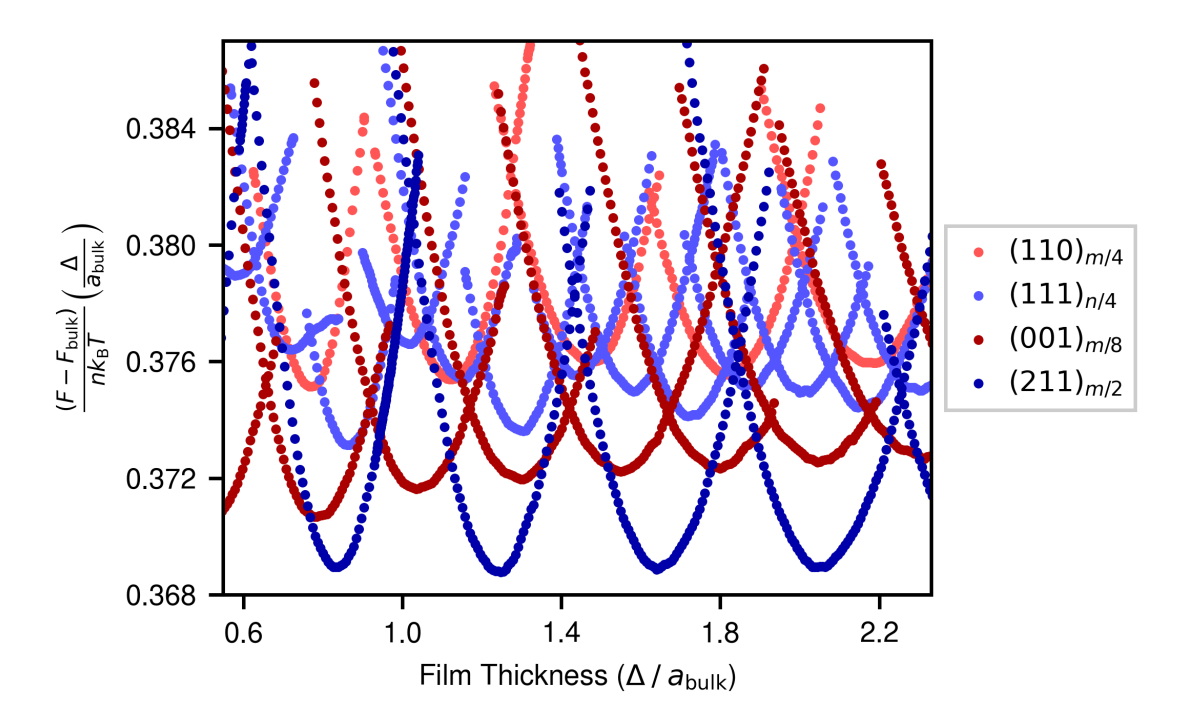


Figure S7: Free energy diagram equivalent to Figure 2 in the main text, but with each individual SCFT calculation shown as a dot on the diagram.

6 Other boundary effects in double-gyroid films

In the main text, we claim that boundary frustration is the only boundary effect that can explain the relative stability of different orientations of DG, because the differences cannot be explained using the other known boundary effects. Here, we show calculations that support this claim, comparing the four films shown in Figure 1 of the main text. In particular, the two boundary effects that must be discussed are 1) the entropic preference for the minority block to be located against the wall, and 2) the negative line tension that occurs at all points where the A/B interface intersects the wall. The other boundary effects — preferential wetting and commensurability of the film thickness — are not relevant to this discussion because the films described in the main text have non-preferential walls and the film thickness is varied in order to identify the most commensurate thicknesses.

To quantify the strength of the first boundary effect in each of the four films being compared, we calculate the fraction of species A that exists on the polymer/wall interface for each. More specifically, we calculate the average value $\langle \phi_A^* \rangle$ across the entire polymer/wall interface, where $\phi_A^*(\mathbf{r}) = \phi_A(\mathbf{r})/[\phi_A(\mathbf{r}) + \phi_B(\mathbf{r})]$ is the fraction of polymer at position \mathbf{r} that is species A, and where we define the polymer/wall interface to be the plane at which $\phi_m = 0.5$. The results are shown in Figure S8a. The orientations are listed in the order of their stability, with the most stable orientation on the bottom. Clearly, the amount of species A is not predictive of the stability of each orientation, because the most unstable orientation has the largest amount of species A at the wall. Note that we must use ϕ_A^* rather than ϕ_A because the total polymer density is reduced near the wall, such that $\phi_A(\mathbf{r}) + \phi_B(\mathbf{r}) < 1$, and the use of ϕ_A^* removes the effect of this reduced polymer density.

Next, we quantify the strength of the second boundary effect in each of the four films by calculating the length of the line along which the A/B interface and the wall intersect, which we will call L_{wall}^{AB} . The A/B interface is defined as the surface on which $\phi_A = \phi_B$, and the polymer/wall interface is again defined to be the plane at which $\phi_m = 0.5$. In order to properly compare the different films to one another, we must divide each length by the

corresponding area of the surface A_{wall} , since this area is different for each film. Therefore, the property that we wish to compare is the length of contact between the A/B interface and the wall per unit area of the film, $L_{\text{wall}}^{\text{AB}}/A_{\text{wall}}$. We nondimensionalize this result by multiplying by a factor of $N^{1/2}b$, the unperturbed root-mean-squared end-to-end distance of the polymer. The results are shown in Figure S8b. As with the results of Figure S8a, the relative stability of each orientation cannot be explained based on the results of the figure, which supports the claim from the main text that boundary frustration is the dominant boundary effect for determining the relative stability of different orientations of double gyroid.

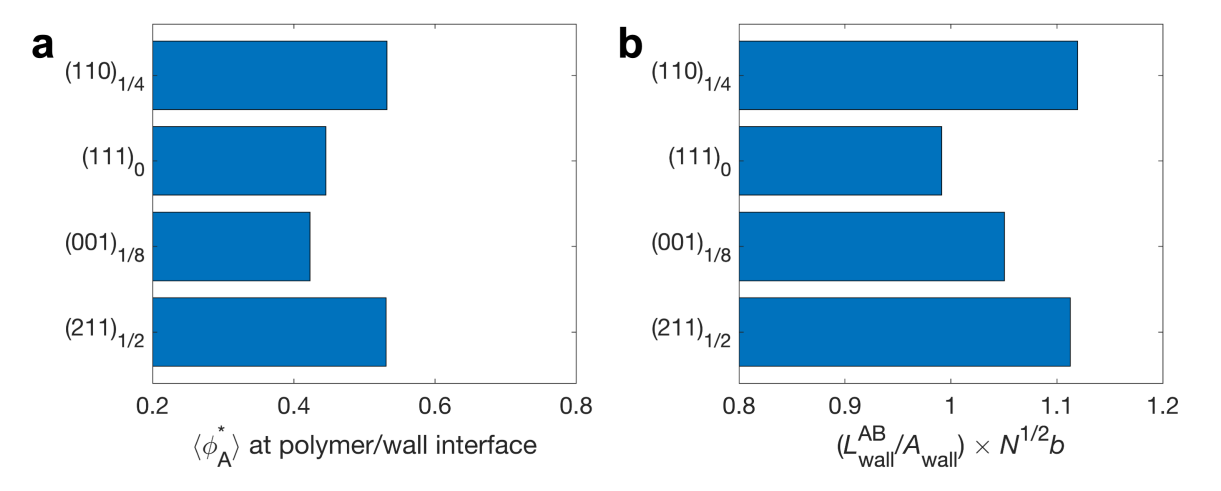


Figure S8: The strength of different boundary effects in each of the four films shown in Figure 1 of the main text. a) The fraction of the polymer/wall interface that is occupied by species A, calculated as the average $\langle \phi_A^* \rangle$ of the fraction of polymer that is species A, $\phi_A^* = \phi_A/(\phi_A + \phi_B)$. b) The length L_{wall}^{AB} of the line along which the A/B interface and the wall intersect per unit area of the thin film, nondimensionalized by a factor of $N^{1/2}b$. Note that, in both bar charts, the x-axis does not start at zero; this is for visualization purposes.

7 Calculating the wetting angle

Defining an exact wetting angle is nontrivial in computational models with a polymer/wall interface of finite width, since a wetting angle is defined only against a perfectly rigid boundary. Different interface widths will result in slight variations in the observed wetting angle, even when all other system parameters are held the same. However, test calculations that we performed with a different interface width indicate that the observed trends discussed in this work remain similar regardless of the polymer/wall interface width.

To define a wetting angle, we must define a Gibbs dividing surface: a plane parallel to the wall, somewhere within the polymer/wall interface, that represents the point where the wall "begins" for the purposes of calculating the wetting angle. ¹³ The observed wetting angle will vary somewhat depending on the location of this dividing surface. ¹³ Here, the sigmoidal shape of our mask density (Equation 3) lends itself well to a choice of dividing surface at $\phi_m = 0.5$, which is the midpoint of the sigmoid and thus the middle of the polymer/wall interface. We also must define another dividing surface between A and B domains, which we choose here to be the surface at which $\phi_A = \phi_B$. The intersection of this A/B dividing surface and the polymer/wall dividing surface is the value we use as the wetting angle.

To calculate the wetting angle at a given point of intersection between the A/B interface and the wall, we first need to identify the A/B interface, the surface at which $\phi_A = \phi_B$. To do this, we use MATLAB's isosurface function. isosurface takes the values of a function on a 3D mesh as an input, and uses interpolation to compute a 3D surface on which the function is equal to a specified isovalue. The 3D surface computed by isosurface is a mesh of small triangles. By passing the field $\phi_A - \phi_B$ into the isosurface function with an isovalue of zero, we construct a triangulated mesh representing the A/B interface.

As an additional step to ensure consistency, we also choose a wall thickness for our SCFT calculation that places gridpoints exactly on the polymer/wall interface (the plane where $\phi_m = 0.5$). We then delete all data on gridpoints at which $\phi_m < 0.5$ before computing the isosurface. The benefit of performing these steps is that the resulting triangulated mesh

will terminate at the polymer/wall interface, and does not contain any triangles that are "inside" the wall or that cross the polymer/wall interface. This means that the triangles nearest the wall have an edge that is coplanar with the plane $\phi_m = 0.5$. These triangles are then used to compute the wetting angle at each point.

We also note that the size of some triangles is larger than others, so they must be properly weighted in order to compute the distribution of wetting angles across the entire polymer/wall interface. In the wetting angle distributions calculated herein (Figures 4 and S9), the contribution of each triangle is weighted according to the length of the edge that it shares with the plane $\phi_m = 0.5$.

8 Wetting angles in other candidate phases

As mentioned in the main text, for non-preferential walls, we observe similar wetting angles across all phases and orientations tested. This is demonstrated in the Figure S9 below. The film thickness of each structure was chosen to be a thickness that represents a local free-energy minimum (i.e., a thickness at which the structure is minimally strained along the direction normal to the film).

The perforated-lamellar phase is the only phase with an average wetting angle that is significantly different from 85°. We attribute this to the fact that the point of intersection between the wall and the A/B interface in this phase is located on the perforations in the lamellae, which are regions with quite high local packing frustration.¹⁴

We also include the corresponding angle distributions for four planes in the bulk double-gyroid morphology, corresponding to the four most stable termination planes found in our thin film calculations: $(211)_{1/2}$, $(110)_{1/4}$, $(111)_0$, and $(001)_{1/8}$. These distributions are shown in Figure S10.

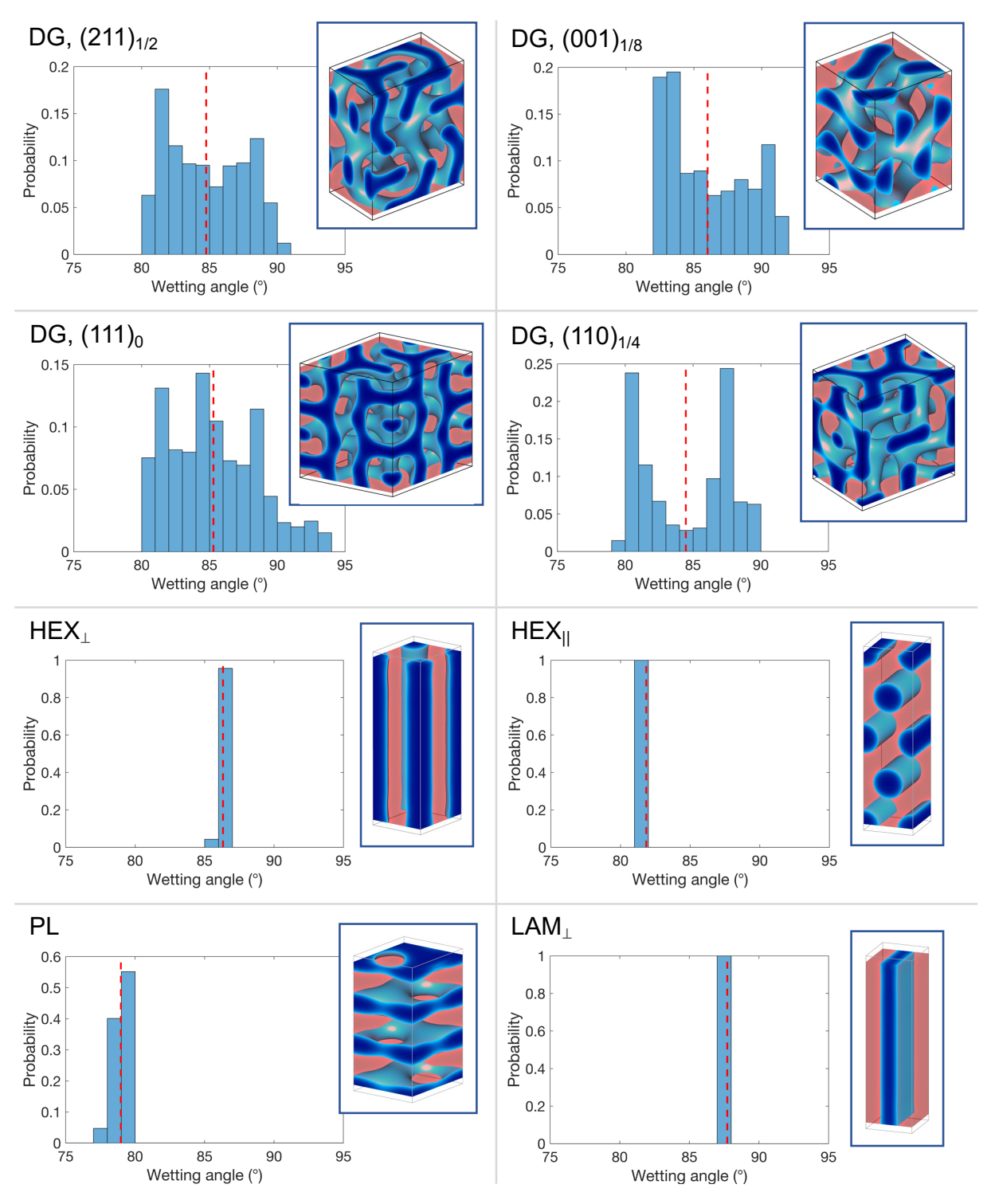


Figure S9: Wetting angle distribution for thin films in various phases containing a polymer with $f_{\rm A}=0.36$ and $\chi N=20$, confined between non-preferential walls. Red lines indicate the average wetting angle. HEX = hexagonally packed cylinders, PL = perforated lamellae, and LAM = lamellae.

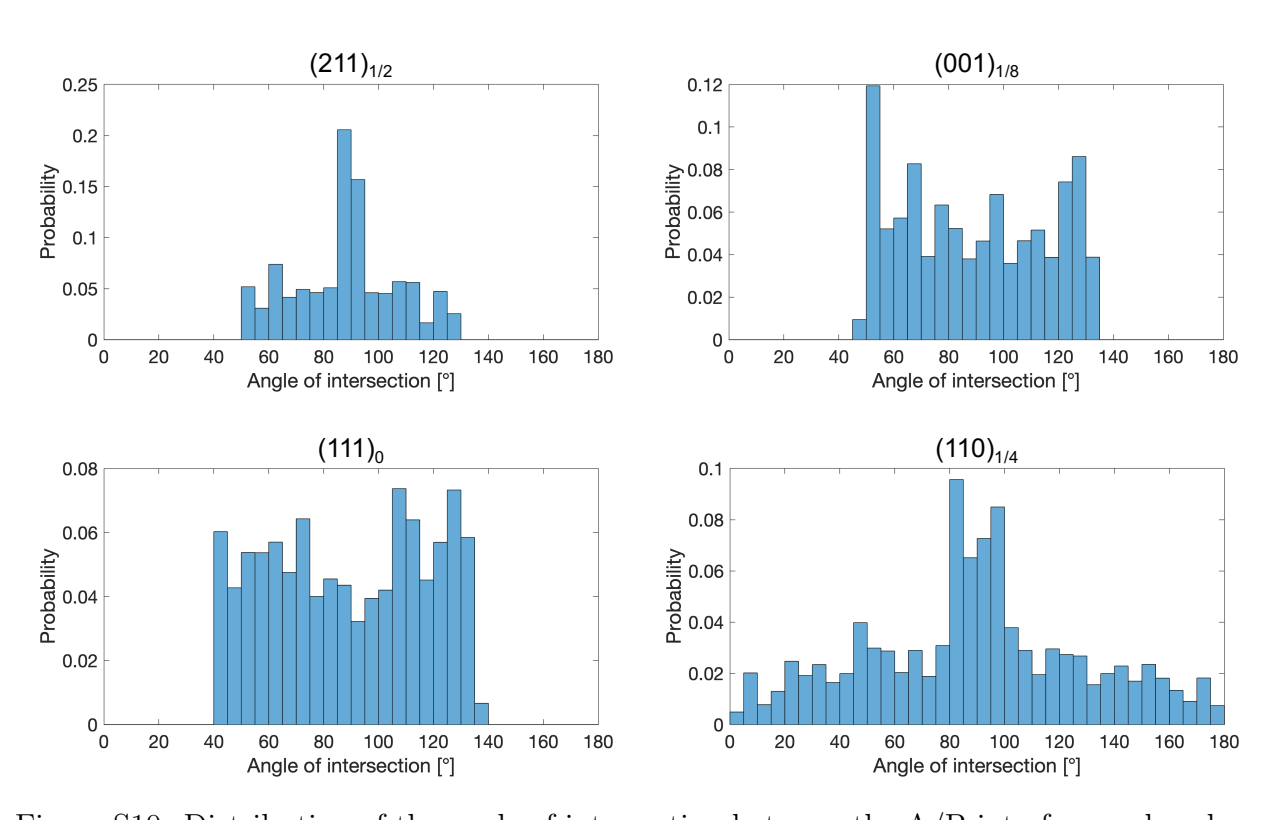


Figure S10: Distribution of the angle of intersection between the A/B interface and a plane through the bulk double-gyroid phase at $f_A = 0.36$ and $\chi N = 20$. The title of each panel indicates the plane.

9 Construction of Figure 3

Figure 3 in the main text was constructed using a very similar technique to that used to calculate the wetting angle, as described in Section 7. First, an isosurface was constructed to represent the A/B interface as a triangulated mesh, considering only the regions of the unit cell in which $\phi_m \geq 0.5$. As in Section 7, we define the isosurface as the surface on which $\phi_A = \phi_B$, and construct the surface using MATLAB's isosurface function.

The heat maps of Figure 3 in the main text are 2D histograms, in which each pixel represents a bin. To represent the bulk morphology, we used the thin film initial guesses that we constructed from the bulk morphology, since the initial guesses had already been rotated/truncated for that particular orientation. This allowed us to use the same procedure for both the bulk morphology and the thin films, since the data were in the same form. To create the histograms, each triangle of the isosurface was sorted into a bin based on its height z and its angle relative to the wall. The z-value of each triangle was computed based on the average height of the three vertices above the bottom wall. Each triangle's contribution to its respective bin was weighted based on the area of the triangle, since some triangles on the mesh are significantly larger than others. Once all triangles were sorted into bins, the histogram was normalized so that the sum of all bins adds to 1.

10 Wetting angles at $f_A = 0.5$

In the main text, we assert that the entropic preference for the minority species to be located against the wall causes an effective reduction of the interfacial tension between the minority block and the wall. This reduction of interfacial tension causes the optimal wetting angle to be $< 90^{\circ}$ when $f_{\rm A} < 0.5$. To further support this claim, we performed SCFT calculations at $f_{\rm A} = 0.5$ for two orientations of double-gyroid thin films, and calculated the wetting angle distributions. There is no minority block when $f_{\rm A} = 0.5$, so there is no entropic preference for either block to be located against the wall, and the optimal wetting angle is expected to be 90° . The results are shown in Figure S11. It is evident that the wetting angles are now distributed around an angle of about 90° , as compared to the results shown in Figure S9 where the wetting angles are distributed around an angle of about 85° .

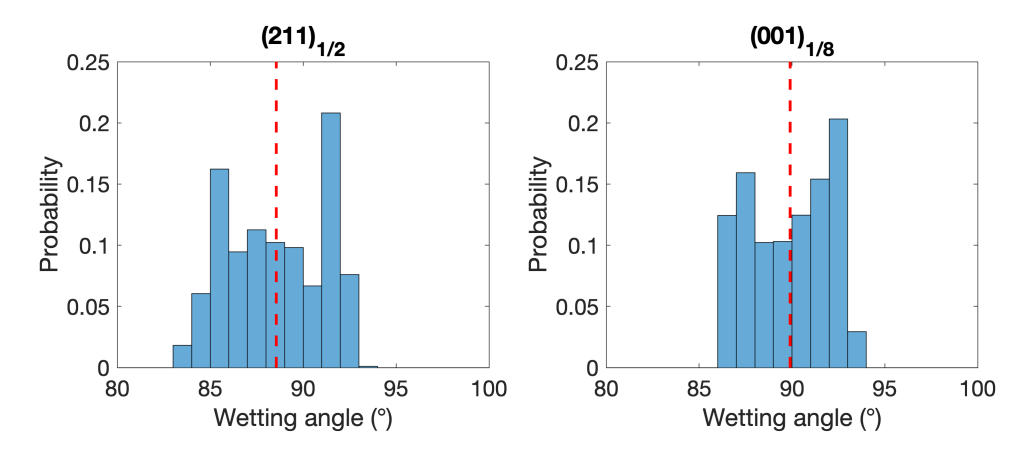


Figure S11: Wetting angle distribution for thin films of double-gyroid with $(211)_{1/2}$ and $(001)_{1/8}$ termination planes, for films containing a polymer with $f_A = 0.50$ and $\chi N = 20$ confined between non-preferential walls. Red lines indicate the average wetting angle for each film.

References

- (1) Cheong, G. K.; Chawla, A.; Morse, D. C.; Dorfman, K. D. Open-Source Code for Self-Consistent Field Theory Calculations of Block Polymer Phase Behavior on Graphics Processing Units. Eur. Phys. J. E 2020, 43, 15.
- (2) Fredrickson, G. H. *The Equilibrium Theory of Inhomogeneous Polymers*; Oxford University Press: Oxford, 2006.
- (3) Arora, A.; Qin, J.; Morse, D. C.; Delaney, K. T.; Fredrickson, G. H.; Bates, F. S.; Dorfman, K. D. Broadly Accessible Self-Consistent Field Theory for Block Polymer Materials Discovery. *Macromolecules* 2016, 49, 4675–4690.
- (4) Arora, A.; Morse, D. C.; Bates, F. S.; Dorfman, K. D. Accelerating Self-Consistent Field Theory of Block Polymers in a Variable Unit Cell. J. Chem. Phys. 2017, 146, 244902.
- (5) Matsen, M. W. Thin Films of Block Copolymer. J. Chem. Phys. 1997, 106, 7781–7791.
- (6) Huang, C.; Zhu, Y.; Man, X. Block Copolymer Thin Films. *Phys. Rep.* **2021**, *932*, 1–36.
- (7) Khanna, V.; Cochran, E. W.; Hexemer, A.; Stein, G. E.; Fredrickson, G. H.; Kramer, E. J.; Li, X.; Wang, J.; Hahn, S. F. Effect of Chain Architecture and Surface Energies on the Ordering Behavior of Lamellar and Cylinder Forming Block Copolymers. *Macromolecules* 2006, 39, 9346–9356.
- (8) Gottlieb, D.; Orszag, S. A. Numerical Analysis of Spectral Methods: Theory and Applications, nachdr. ed.; CBMS-NSF Regional Conference Series in Applied Mathematics 26; Soc. for Industrial and Applied Mathematics: Philadelphia, Pa, 1977.
- (9) Tzeremes, G.; Rasmussen, K. Ø.; Lookman, T.; Saxena, A. Efficient Computation of the Structural Phase Behavior of Block Copolymers. *Phys. Rev. E* **2002**, *65*, 041806.

- (10) Ranjan, A.; Qin, J.; Morse, D. C. Linear Response and Stability of Ordered Phases of Block Copolymer Melts. *Macromolecules* **2008**, *41*, 942–954.
- (11) Wu, Y.-H.; Lo, T.-Y.; She, M.-S.; Ho, R.-M. Morphological Evolution of Gyroid-Forming Block Copolymer Thin Films with Varying Solvent Evaporation Rate. *ACS Appl. Mater. Interfaces* **2015**, *7*, 16536–16547.
- (12) Antoine, S.; Aissou, K.; Mumtaz, M.; Telitel, S.; Pécastaings, G.; Wirotius, A.-L.; Brochon, C.; Cloutet, E.; Fleury, G.; Hadziioannou, G. Core-Shell Double Gyroid Structure Formed by Linear ABC Terpolymer Thin Films. *Macromol. Rapid Commun.* 2018, 39, 1800043.
- (13) Hur, S.-M.; García-Cervera, C. J.; Fredrickson, G. H. Chebyshev Collocation in Polymer Field Theory: Application to Wetting Phenomena. *Macromolecules* 2012, 45, 2905–2919.
- (14) Matsen, M. W.; Bates, F. S. Origins of Complex Self-Assembly in Block Copolymers.

 *Macromolecules 1996, 29, 7641–7644.